



Full Length Article

Role of solute elements in Mg-Mg₂Ni hydrogen storage alloys: A first-principles calculation study

Min-Seok Yoon^a, Jae Hur^a, Seo-Hui Park^a, Ui-Jong Lee^a, Guanglong Xu^b, Hyung-Ki Park^c, Byeong-Chan Suh^{d,*}, Young Min Kim^{d,e,*}, Won-Seok Ko^{a,*}

^aDepartment of Materials Science and Engineering, Inha University, Incheon 22212, Republic of Korea

^bCollege of Materials Science and Engineering, Nanjing Tech University, Nanjing 211816, China

^cFunctional Materials and Components R&D Group, Korea Institute of Industrial Technology, Gangneung 25440, Republic of Korea

^dAdvanced Metals Division, Korea Institute of Materials Science, Changwon 51508, Republic of Korea

^eAdvanced Materials Engineering, University of Science and Technology, Daejeon 34113, Republic of Korea

Received 8 September 2024; received in revised form 16 November 2024; accepted 18 November 2024

Available online 4 December 2024

Abstract

The effects of various alloying elements on the performance of Mg-Mg₂Ni hydrogen storage alloys were investigated by performing first-principles density functional theory calculations. We examined the important characteristics of hydrogen storage alloys by considering both Mg-based solid solution and Mg₂Ni-based intermetallic compound phases, where the hydride forms are MgH₂ and Mg₂NiH₄, respectively. In particular, qualitatively valid information for predicting changes in plateau pressures in the pressure-composition-temperature (PCT) curve was provided by calculating changes in the energy of related hydrogenation reactions. The effects of alloying elements on volume changes due to hydrogenation reactions were also obtained to provide additional criteria for the practical use of hydrogen storage alloys. For the Mg₂Ni-based intermetallic compound, we examined the site preference of each alloying element, considering the designated stoichiometry of the base alloy. Based on the revealed site preferences, the effects of various possible alloying elements on the properties of Mg₂Ni-based hydrides were also examined. Electronic structure analyses were further conducted to elucidate the detailed mechanisms underlying the role of the additional solute elements.

© 2024 Chongqing University. Publishing services provided by Elsevier B.V. on behalf of KeAi Communications Co. Ltd.

This is an open access article under the CC BY-NC-ND license (<http://creativecommons.org/licenses/by-nc-nd/4.0/>)

Peer review under responsibility of Chongqing University

Keywords: Mg-Mg₂Ni alloys; Density functional theory; Hydrogen storage alloys; Metal hydrides.

1. Introduction

Considering utilizing non-renewable energy sources, such as fossil fuels, has depleted energy resources and caused environmental pollution, hydrogen has attracted increasing attention as a renewable energy source. To enhance the hydrogen economy, developing technologies that realize the efficient and safe storage and transportation of hydrogen is highly desirable. Among several possible hydrogen storage technologies, the storage of hydrogen in the solid state, such

as using hydrogen storage alloys, has attracted much attention owing to its high storage capacity and superior safety compared to other storage technologies [1–5]. In particular, Mg alloys are considered promising hydrogen storage materials owing to their lightweight, low cost, and high hydrogen storage capacity (~7.62 wt.%) properties [6,7]. For example, pure Mg reacts with hydrogen to form magnesium hydride (MgH₂), which enables the transportation of large amounts of hydrogen under ambient conditions.



However, MgH₂ itself is not a promising hydrogen storage material because it forms strong bonds with hydrogen ($\Delta H = \sim -74.5 \text{ kJ/mol H}_2$) [8,9], making the dehydrogena-

* Corresponding authors.

E-mail addresses: bcsuh@kims.re.kr (B.-C. Suh), ymkim@kims.re.kr (Y.M. Kim), wonsko@inha.ac.kr (W.-S. Ko).

tion process too challenging [10–13]. To enhance the dehydrogenation process of MgH₂, recent studies have focused on ways to improve both the thermodynamic and kinetic properties. For instance, it was reported that combining LiBH₄ and YNi₅ with MgH₂ can significantly enhance hydrogen storage properties, achieving a reversible hydrogen storage capacity of 6.42 wt.% after 110 cycles at 300 °C [14]. The formation of in-situ phase such as MgNi₃B₂ was identified as a critical factor in accelerating dehydrogenation kinetics while maintaining high storage performance [14]. Moreover, the development of one-step approaches for hydrogen generation, storage, transportation, and application without the need for hydrogen compression has been actively explored [15–17]. In particular, hydrogen storage techniques using Mg or MgH₂ as a reduction agent show significant potential to simplify systems and reduce costs. For example, previous studies reported that the use of Mg/MgH₂ for Li(Na)BH₄ regeneration provides a unified solution for hydrogen storage and generation [18,19]. These innovative Mg-based hydrogen storage technologies play a crucial role in promoting the use of hydrogen as a next-generation clean energy source, providing essential solutions for efficient and safe energy storage.

The performance of hydrogen storage alloys is generally ascertained by examining pressure-composition-temperature (PCT) curves. The PCT curve illustrates the hydrogen storage capacity, temperature, and pressure at which a material can be operated. Thus, the relevant control of the PCT curve is an important requirement in the practical implementation of hydrogen storage alloys. However, MgH₂ hydrides require extremely low desorption pressures or high temperatures above 325 °C to release hydrogen when reverting to pure Mg.

To address this issue, numerous studies have been conducted [6,20–28] based on including alloying [6,29–32] and catalytic addition [33,34], and the partial substitution of Mg with other elements is considered the most promising route to decrease the stability of hydrides. For example, adding transition metals to Mg can effectively weaken the interactions between Mg and H, forming intermetallic compounds [8]. Among the possible choices for an additional element in the binary combination, the most notable is Ni. For example, Shen et al. [35] demonstrated that using nano-sized catalysts like ultrafine Ni can significantly enhance the kinetics and reversible hydrogen storage capacity of MgH₂-based composites. Moreover, the incorporation of Ni was reported to reduce the dehydrogenation activation energy by up to 26.9 % compared to pure Mg, enabling more efficient hydrogen release even at lower temperatures [35–38]. As shown in the binary Mg-Ni phase diagram [39], the Mg-Ni system involves two intermetallic compounds (*e.g.*, Mg₂Ni and MgNi₂). Among various possible compositions of the Mg-Ni binary alloy, the Mg-rich compositions within the two-phase stable region with hcp solid solution phase and the Mg₂Ni compound have attracted much attention because the Mg₂Ni can contribute to improving the hydrogen desorption kinetics and reduce the hydrogen desorption temperature to be ~250 °C [40]. The Mg₂Ni compound alone can be another hydrogen storage alloy because it can form a stable hydride (Mg₂NiH₄) via the

following reaction [12,41–43].



The dehydrogenation process of Mg₂Ni alloys has been considerably improved compared to that of existing Mg-based hydrogen storage alloys. With the appropriate selection of composition and processing conditions, a lamellar eutectic mixture with an Mg-rich hcp solid solution and Mg₂Ni compound phases can be readily formed. The Mg-Mg₂Ni eutectic structure with finely distributed interfaces facilitated the dissociation of hydrogen molecules and the penetration of hydrogen atoms [44]. Thus, adding Ni forms a secondary phase that acts as a ‘hydrogen pump’ during dehydrogenation process [7,45–47].

However, challenges remain in the development of practical Mg-Mg₂Ni hydrogen storage alloys, such as an overall increase in the hydrogen storage capacity because the Mg₂Ni-based hydride exhibits a lower hydrogen storage capacity (~3.6 wt.%) [48] than the Mg-based hydride (~7.62 wt.%) [49]. Moreover, as the Mg₂Ni still exhibits a comparably high stability of hydride phase ($\Delta H = -64 \text{ kJ/mol H}_2$), the stability of the hydride could be further decreased to achieve optimal performance [50]. In particular, the dual tuning of thermodynamic and kinetic properties through alloying processes has emerged as a key solution to overcome these challenges [14]. Therefore, considering additional ternary alloying elements is highly desirable for the practical application of Mg-Mg₂Ni hydrogen storage alloys, and several experimental studies were performed in this direction [6,38,51,52]. However, designing multicomponent alloys within the vast realm of the compositional space only via experiments can be challenging. In particular, adding alloying elements can change the properties of the Mg-rich solid solution phase (*i.e.*, MgH₂ hydride) as well as the properties of Mg₂Ni compounds (*i.e.*, Mg₂NiH₄ hydride) to different degrees; however, there is not enough information on the specific roles of various alloying elements.

First-principles density functional theory (DFT) calculations can be an ideal method to supplement experiments by determining the effects of alloying elements on properties related to the hydrogen storage. For example, Kelkar et al. [26] utilized the DFT calculation to predict the effect of additional Al and Si on the hydrogen adsorption properties of MgH₂ hydrides and reported that adding Al and Si destabilizes the hydride and enhances its dehydrogenation properties. Similarly, Hussain et al. [27] investigated the doping effect of transition metals (Al, Ti, Fe, Ni, Cu, and Nb) to modulate the thermodynamic stability of MgH₂ hydrides. Adding elements to Mg alloys effectively reduced the dehydrogenation temperature and stability of the hydride. In the case of the Mg₂Ni-based hydrogen storage alloys, several DFT studies have explored the effects of alloying elements. For example, Liu et al. [53] examined the effect of substitutional Si on the stability of Mg₂NiH₄ hydrides and reported that adding Si destabilized the hydrides. Li et al. [24] reported that when Y atoms occupy Mg sites, the stability of the Mg₂NiH₄ hydride is decreased. Zeng et al. [25] examined the doping effect of

Ag and Al and reported that substitutional Ag and Al atoms at the Mg sites can destabilize the Mg_2NiH_4 hydride.

Although several DFT studies have been performed for selected alloying elements, systematic analysis of the role of each solute element in Mg - Mg_2Ni hydrogen storage alloys remains lacking. In this study, we conducted comprehensive DFT calculations for a wide range of alloying elements to provide substantial data for further alloying design processes. In particular, identifying possible substitution positions (*i.e.*, site preferences) of solute elements in the Mg_2Ni structure was prioritized because they significantly determine the overall substitutional effects. Once the site preference of the solute elements was determined, the enthalpy of the hydrogenation reaction was calculated to ascertain the effect of the solute elements on the changes in the PCT curve. Furthermore, the volume change of the hydrogen storage alloy due to the hydrogenation reaction, an additional factor to be considered in the practical alloying design process, was determined. Finally, the effects of the alloying elements on the electronic properties and bonding characteristics were examined to gain more detailed insights into the influence of solute elements on the hydrogen storage properties. The results of this study are expected to provide qualitatively valid information for designing new Mg - Mg_2Ni hydrogen storage alloys with appropriate performance for the required applications.

2. Methodology

DFT calculations were performed using the Vienna ab initio simulation package (VASP) code within the projector-augmented wave (PAW) method [54,55]. The exchange-correlation function was described utilizing the generalized gradient approximation (GGA) and the Perdew–Burke–Ernzerhof method [56,57]. A cutoff energy of 360 eV was selected for the plane-wave basis set considering reasonable convergence and computational efficiency. The Brillouin zone was sampled via the Methfessel–Paxton smearing method, with a smearing width of 0.1 eV [58]. A relevant set of Γ -centered k -point meshes, a density of approximately 9000 k -points per reciprocal atom, was employed for each type of supercell, as summarized in Table 1. The selection of these k -point meshes was based on convergence tests, where all supercells achieved energy convergence within an energy difference of $<10^{-5}$ eV/atom, confirming that the selected k -point densities are sufficient for accurate energy calculations related

to target properties. We also confirmed that this selection ensures reliable and consistent results for electronic property calculations. All the DFT calculations were performed with full relaxation of the atomic positions and cell parameters (*i.e.*, the dimensions and angles of the supercell). Each structure was optimized under a convergence criterion of 10^{-6} eV and 10^{-2} eV/Å for energy and force, respectively.

While various elements of the periodic table (Ag, Al, As, Au, Ba, Be, Bi, Ca, Cd, Ce, Co, Cr, Cs, Cu, Fe, Ga, Gd, Ge, Hf, Hg, In, Ir, K, La, Li, Mg, Mo, Na, Nb, Nd, Ni, Os, P, Pb, Pd, Pt, Rb, Re, Rh, Ru, S, Sb, Sc, Se, Si, Sn, Sr, Ta, Tc, Te, Tl, V, W, Y, Zn, and Zr) were considered as candidates, only the impact of substitutional solute elements was considered, with interstitial forms excluded considering the storage capacity of hydrogen. Inert gases, halogens, radioactive elements, and several rare earth elements were excluded. Pseudopotentials recommended by the VASP library were used in the calculations. In the present study, zero-point vibration contributions to the energy values were not considered because the objective was to provide qualitatively valid information for the rapid screening of candidate elements rather than providing quantitative data.

As aforementioned, Mg -based hydrogen storage alloys are associated with a hydride form of MgH_2 under the hydrogen charging condition. Fig. 1 shows a schematic of pure Mg and MgH_2 hydride structures used in the present DFT calculations. Depending on temperature and pressure conditions, MgH_2 can crystallize as either α - MgH_2 or γ - MgH_2 . Under the ambient conditions, a stable one is the rutile-type α - MgH_2 structure, which has a crystal structure of tetragonal $P4_2/mnm$ (space group No 136). The unit cell contains two Mg and four H atoms while the Mg^{2+} ion forms a bond with six equivalent H^{1-} ions to create a mixture of MgH_6 octahedral (Fig. 1). This local structure involves two shorter (1.93 Å) and four longer (1.94 Å) Mg - H bonds [59]. Supercells with 96 atoms (*i.e.*, 32 Mg and 64 H atoms), generated by a $2 \times 2 \times 4$ duplication of the unit cell with six atoms, were used to calculate the related properties.

When a pressure higher than ~0.39 GPa is applied, α - MgH_2 transforms into the γ - MgH_2 , which has a α - PbO_2 -type crystal structure of orthorhombic $Pbcn$ (space group No 60) [59–61]. The unit cell contains four Mg and eight H atoms, where the H^{1-} ions bonded with three equivalent Mg^{2+} ions in a triangular plan as shown in Fig. 1. In other words, there are three different types of Mg - H bonds in this structure, each of

Table 1
Information on atomic structures and corresponding k -point meshes used in the present DFT calculation.

Structure	Space group	Purpose	Number of atoms			k -points	
			Total	Mg	Ni		
hcp Mg	$P6_3/mmc$	Volume expansion, enthalpy of reaction	32	32	–	–	$7 \times 7 \times 6$
α - MgH_2	$P4_2/mnm$	Volume expansion, enthalpy of reaction	96	32	–	64	$5 \times 5 \times 4$
γ - MgH_2	$Pbcn$	Volume expansion, enthalpy of reaction	96	32	–	64	$5 \times 4 \times 4$
Mg_2Ni	$P6_222$	Site preference, volume expansion, enthalpy of reaction	72	48	24	–	$6 \times 6 \times 4$
Mg_2NiH_4	$C2/c$	Volume expansion, enthalpy of reaction	168	48	24	96	$3 \times 7 \times 3$
		Density of states, electron localization function	168	48	24	96	$7 \times 9 \times 7$

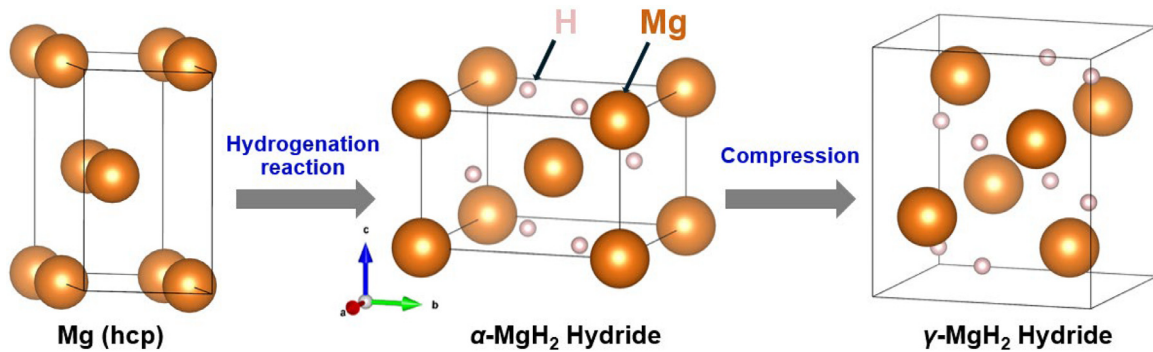


Fig. 1. Schematic illustration of hcp Mg, α -MgH₂, and γ -MgH₂ structures used in the present DFT calculations.

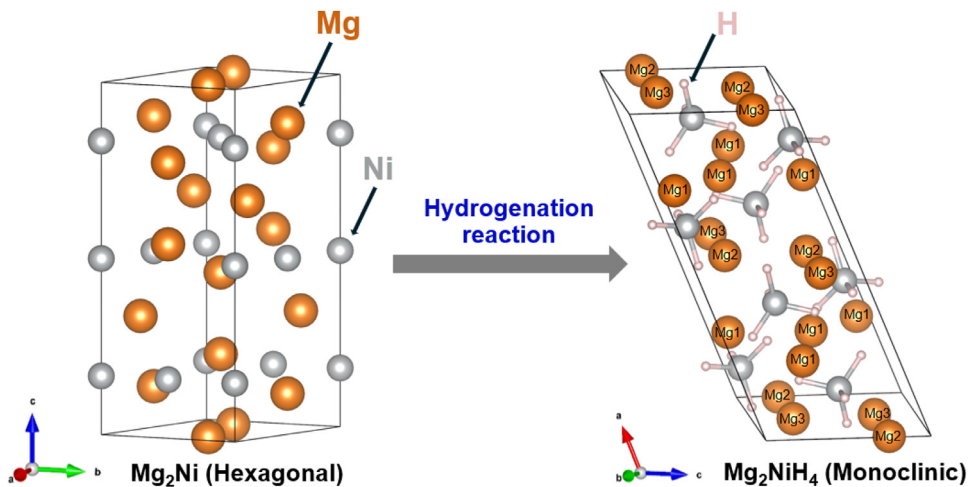


Fig. 2. Schematic illustration of Mg₂Ni and Mg₂NiH₄ structures used in the present DFT calculations.

which has a Mg-H bond length in the range of 1.90–1.99 Å. To apply the same conditions as in α -MgH₂, a $2 \times 2 \times 2$ duplication of the unit cell was performed. In this study, supercells with a total of 96 atoms (*e.g.*, Mg₃₂H₆₄ and Mg₃₁X₁H₆₄) for MgH₂ hydrides and those with a total of 32 atoms for pure Mg (*e.g.*, Mg₃₂) and solid solutions (*e.g.*, Mg₃₂ and Mg₃₁X₁) were consistently used to examine the influence of solute elements.

Mg₂Ni has a crystal structure of hexagonal P6₂22 (space group No 180) [62]. As shown in Fig. 2, the unit cell of Mg₂Ni contains 12 Mg atoms and 6 Ni atoms. In this study, a supercell containing 72 metal atoms, constructed by a $2 \times 2 \times 1$ duplication of the unit cell, was used for further investigation. Mg₂NiH₄ exhibits intriguing phase transformation characteristics. At temperatures above 510 K, the high-temperature (HT) cubic structure is maintained. At temperatures below 510 K, it transforms into two low-temperature (LT) structures. The first is a monoclinic LT1 structure and the second is a twinned orthorhombic LT2 structure [63]. Among these LT hydrides, the present study focuses on the more thermodynamically stable LT1 phase, which has a crystal structure of C2/c (space group No 15) [64]. As shown in Fig. 2, the unit cell of Mg₂NiH₄ contains 16 Mg atoms, 8 Ni atoms, and 32 H atoms. Supercells containing 72 metal atoms and 96

H atoms, constructed by a $1 \times 1 \times 3$ duplication of the unit cell, were used for further examination to match the number of atoms between the hydride and the corresponding base alloy configurations.

In the case of the Mg₂Ni compound, the position of the solute atom in the sublattice structure critically determines the related properties. To understand the influence of each solute element, we used supercells with a solute atom in different sublattices, *e.g.*, Mg₄₇X₁Ni₂₄ and Mg₄₇X₁Ni₂₄H₉₆ configurations for the substitution of a Mg site and Mg₄₈Ni₂₃X₁ and Mg₄₈Ni₂₃X₁H₉₆ configurations for the substitution of a Ni site. The present study aims to provide only the qualitative effect of alloying elements on the properties, considering the substitution of only one atom in a supercell, without considering the detailed concentration effect. As shown in Fig. 2, a solute atom can be substituted at a single Ni site or three different Mg sites (Mg1, Mg2, and Mg3). Therefore, we treated these three Mg sites separately in the property calculations and derived an average value for further examination.

To validate the reliability of the present DFT calculations, the optimized structural parameters of hcp Mg, α -MgH₂, γ -MgH₂, Mg₂Ni, and Mg₂NiH₄ structures were compared with the experimentally reported values as listed in Table 2. The obtained results were consistent with the experimen-

Table 2

Structural parameters of hcp Mg, α -MgH₂, γ -MgH₂, Mg₂Ni, and Mg₂NiH₄ phases predicted by the present DFT calculations compared with reported experimental values.

Structure	Method	<i>a</i> (Å)	<i>b</i> (Å)	<i>c</i> (Å)	(α , β , γ)	Ref.
hcp Mg	DFT	3.195	3.187	5.118	$\alpha = \beta = 90^\circ, \gamma = 120^\circ$	[65]
	Exp.	3.202	3.202	5.200	$\alpha = \beta = 90^\circ, \gamma = 120^\circ$	
α -MgH ₂	DFT	4.483	4.483	3.000	$\alpha = \beta = \gamma = 90^\circ$	[59,66]
	Exp.	4.501	4.501	3.010	$\alpha = \beta = \gamma = 90^\circ$	
γ -MgH ₂	DFT	4.475	4.898	5.401	$\alpha = \beta = \gamma = 90^\circ$	[59,67]
	Exp.	4.505	4.916	5.419	$\alpha = \beta = \gamma = 90^\circ$	
Mg ₂ Ni	DFT	5.194	5.194	13.200	$\alpha = \beta = 90^\circ, \gamma = 120^\circ$	[68,69]
	Exp.	5.200	5.200	13.162	$\alpha = \beta = 90^\circ, \gamma = 120^\circ$	
Mg ₂ NiH ₄	DFT	14.249	6.363	6.438	$\alpha = \gamma = 90^\circ, \beta = 113.18^\circ$	[70–73]
	Exp.	14.343	6.404	6.483	$\alpha = \gamma = 90^\circ, \beta = 113.52^\circ$	

tal data, demonstrating the reliability of the present DFT calculations.

3. Results and discussion

3.1. Energy of hydrogenation reactions of Mg-based storage alloys

Magnesium-based hydrogen storage alloys undergo a spontaneous reaction with hydrogen, as shown in Eq. (1), which is associated with heat dissipation. To improve the practical utility of Mg-based hydrogen storage alloys, it is crucial to tailor the absorption and desorption characteristics of hydrogen in the PCT curve, particularly the location of the plateau pressures. The plateau pressure (P_{eq}) can be calculated using the van't Hoff equation:

$$\ln\left(\frac{P_{eq}}{P_0}\right) = \frac{\Delta H^0}{RT} - \frac{\Delta S^0}{R}, \quad (3)$$

where P_{eq} is the plateau pressure, P_0 is the standard pressure of 1 atm, R is the ideal gas constant, T is the temperature, ΔH^0 is the standard reaction enthalpy, and ΔS^0 is the standard reaction entropy. From Eq. (3), it can be seen that the plateau pressure is influenced by changes of the hydrogenation reaction enthalpy and entropy. For example, a more negative ΔH^0 indicates a lower plateau pressure and the stabilization of the hydride phase, and *vice versa*. However, it is not trivial to derive the exact value of the plateau pressure using DFT calculations alone. This is because of the inherent difficulty of DFT calculations in accurately predicting entropy changes. Alternatively, DFT calculations can be readily performed to obtain the energy difference between the metal and hydride phases at 0 K, closely correlated with the enthalpy change due to hydrogenation reactions. In other words, we can obtain the energy difference between the base alloy and hydride phase at 0 K by DFT calculation, roughly corresponding to the ΔH^0 .

Specifically, we adopted a qualitative approach, where the relative changes in the energy of the hydrogenation reaction (ΔE_r) are used to infer the variation trend of the plateau pressure. In other words, a less negative ΔE_r indicates a reduced stability of the hydride phase, which correlates with an increase in the plateau pressure, indicating that the desorption

of hydrogen is more favorable at lower temperatures. Conversely, a more negative ΔE_r indicates an increased stability of the hydride phase, which correlates with a decrease in the plateau pressure. These trends align with the van't Hoff equation, which shows the correlation between the plateau pressure and reaction enthalpy. Thus, while an exact quantitative prediction of plateau pressures is beyond the scope of the present study, the qualitative trends inferred from ΔE_r provide valuable insights for the alloy design to tune overall hydrogen storage properties. The energy of the hydrogenation reaction from Mg to MgH₂ hydride was examined by DFT calculations using the following equation:

$$\Delta E_r = \frac{E(\text{Mg}_{32}\text{H}_{64}) - E(\text{Mg}_{32}) - 32E(\text{H}_2)}{32}, \quad (4)$$

where $E(\text{Mg}_{32}\text{H}_{64})$ and $E(\text{Mg}_{32})$, the energy values of the hydride and pure Mg, respectively, were obtained from DFT calculations for the supercell structures. The energy value of H₂ molecules, $E(\text{H}_2)$, was obtained by the calculation with a sufficient vacuum region in a cell. Table 3 lists the calculated ΔE_r for the hydrogenation reaction from pure Mg to MgH₂ hydride compared to the reported experimental value and previous calculations. It should be noted that the energy difference at 0 K obtained by DFT calculations does not exactly correspond to the enthalpy change measured experimentally because it can be affected by the temperature. There is an overall discrepancy between the ΔH_r measured by experiments and ΔE_r predicted by usual DFT calculations. Therefore, the primary objective of this study was not to provide the absolute plateau pressure and enthalpy values but rather to predict the relative change in energy due to the hydrogenation reaction with the addition of alloying elements.

To examine the alloying effect, we considered a dilute concentration of solute elements in which a single substitution atom was located in a supercell (*i.e.*, Mg₃₁X₁H₆₄ and Mg₃₁X₁ where X is the solute element), and the ΔE_r values were obtained by applying an equation similar to Eq. (4). Calculations for α -MgH₂ and γ -MgH₂ were independently performed, and results are summarized in Table 4 and Fig. 3. It should be noted that the selected concentration considered in the present study (1/32) would be impractical for some alloying elements due to their very low solubility in Mg. DFT calculations of such a composition are challenging because extremely low

Table 3

Dissociation energy of H₂ molecule, cohesive energy of pure Mg, hydrogenation reaction energies (ΔE_r) of MgH₂ and Mg₂NiH₄ hydrides, and enthalpy of formation (ΔE_f) of Mg₂Ni compound predicted by the present DFT calculations compared with reported experimental and DFT values. For the α -MgH₂ and Mg₂NiH₄ hydride, ΔE_r values per 1 mole of H₂ gas associated with the hydrogenation reactions defined in Eqs. (4) and (12) are presented.

Structure	Property	Experiment	DFT (Previous)	DFT (Present)
H ₂	Dissociation energy of H ₂ molecule (eV)	4.56 ^a	4.56 ^a	4.527
hcp Mg	Cohesive energy (eV)	1.51 ^b	1.53 ^c	1.515
α -MgH ₂	ΔE_r (kJ/mol H ₂)	-74.5 ^d	-55.67 ^d , -62.90 ^e	-52.65
Mg ₂ NiH ₄	ΔE_r (kJ/mol H ₂)	-64 ± 4 ^f	-63.3 ^g , -52.78 ^e	-57.06
Mg ₂ Ni	ΔE_f (kJ/gram-atom)	-17.3 ^h	-17.5 ^h	-17.35

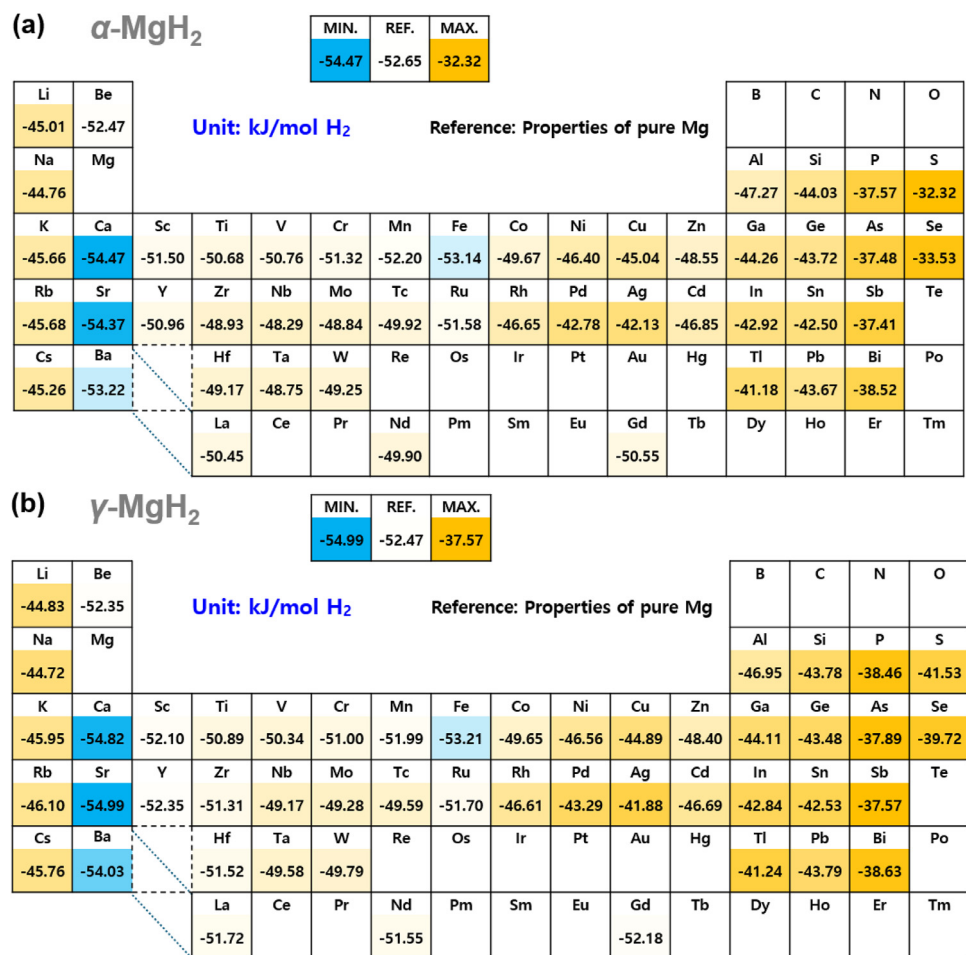
^a Ref. [74].^b Ref. [75].^c Ref. [76].^d Ref. [77].^e Ref. [78].^f Ref. [20].^g Ref. [53].^h Ref. [22].

Fig. 3. Visualization of the effect of additional alloying elements on the energy of hydrogenation reaction (ΔE_r) calculated by Eq. (4). Results of substitution in (a) α -MgH₂ and (b) γ -MgH₂ hydrides are presented.

solubility requires an excessively large supercell. Therefore, the present study provides only qualitatively valid information on the effects of the alloying elements.

Fig. 3 shows the calculated energy values for the hydrogenation reaction. This shows that each solute element affects

the stability of the hydrides differently, but there is a general trend for the hydride phases to become unstable with the addition of solute elements (*i.e.*, an increase in plateau pressures). In particular, group 15 and 16 elements (*e.g.*, P, As, Sb, Bi, S, and Se) exhibited pronounced destabilizing tendencies for

Table 4

Effect of additional alloying elements on the hydrogenation reaction energy (ΔE_r) and volume change (ΔV) of α -MgH₂ and γ -MgH₂ hydrides due to hydrogenation reactions. The calculated values of pristine MgH₂ hydrides are indicated in bold.

Element	α -MgH ₂		γ -MgH ₂	
	ΔE_r (kJ/mol H ₂)	ΔV (%)	ΔE_r (kJ/mol H ₂)	ΔV (%)
—	−52.649	31.804	−52.473	29.395
Ag	−42.131	33.845	−41.878	31.653
Al	−47.273	32.931	−46.946	30.430
As	−37.479	34.026	−37.888	32.433
Ba	−53.221	29.723	−54.033	27.281
Be	−52.469	32.906	−52.352	30.428
Bi	−38.525	32.644	−38.633	30.507
Ca	−54.471	30.755	−54.818	28.057
Cd	−46.846	33.203	−46.689	30.807
Co	−49.673	34.387	−49.647	31.936
Cr	−51.315	33.818	−51.003	31.365
Cs	−45.259	29.456	−45.758	26.589
Cu	−45.045	34.148	−44.890	31.913
Fe	−53.137	33.799	−53.208	31.210
Ga	−44.262	33.585	−44.108	31.172
Gd	−50.553	31.194	−52.184	28.244
Ge	−43.723	34.492	−43.480	32.047
Hf	−49.172	32.908	−51.515	28.550
In	−42.919	33.480	−42.837	31.012
K	−45.660	30.449	−45.955	27.767
La	−50.449	30.359	−51.724	27.984
Li	−45.007	32.518	−44.834	30.240
Mn	−52.203	33.865	−51.993	31.374
Mo	−48.844	34.457	−49.277	29.665
Na	−44.757	31.576	−44.719	29.169
Nb	−48.289	33.829	−49.173	29.076
Nd	−49.904	30.918	−51.546	28.282
Ni	−46.401	34.145	−46.558	32.214
P	−37.572	33.992	−38.460	32.850
Pb	−43.671	33.469	−43.794	30.799
Pd	−42.780	34.901	−43.290	33.020
Rb	−45.681	29.891	−46.100	27.108
Rh	−46.649	35.422	−46.605	33.119
Ru	−51.581	34.964	−51.704	32.347
S	−32.318	32.569	−41.528	31.482
Sb	−37.409	33.301	−37.573	31.279
Sc	−51.498	31.940	−52.100	28.514
Se	−33.529	32.520	−39.716	31.249
Si	−44.029	34.346	−43.778	32.107
Sn	−42.503	34.002	−42.529	31.333
Sr	−54.368	30.030	−54.994	27.390
Ta	−48.753	33.972	−49.581	29.122
Tc	−49.915	34.871	−49.586	32.241
Ti	−50.676	33.185	−50.886	28.680
Tl	−41.185	33.550	−41.243	31.006
V	−50.758	33.690	−50.342	31.133
W	−49.254	34.686	−49.791	29.719
Y	−50.957	31.204	−52.349	28.146
Zn	−48.549	33.115	−48.401	30.709
Zr	−48.930	32.685	−51.311	28.538

the hydride phases. Conversely, adding elements in the same group as Mg (e.g., Ca, Sr, and Ba) was found to lower the hydrogenation reaction energy more than that of MgH₂ hydrides (i.e., decrease in plateau pressures). Comparing the α -MgH₂ and γ -MgH₂ hydrides, we observed no significant difference in the influence of solute elements.

Table 5 presents a comparison between the present DFT predictions and reported experimental results, which enabled us to ascertain our predictions of the impact of the solute element on Mg-based hydrogen storage alloys. Although the solute concentrations differed from the reported experimental results, we could roughly estimate the impact of each solute element. Previous experiments have mostly focused on candidate solute elements that can destabilize MgH₂ hydride. As shown in **Table 5**, all the solute elements considered in previous studies demonstrated destabilization of the hydride phase, which is consistent with the present DFT calculations. The DFT prediction also reproduced the magnitude (i.e., labeled as ‘strong, moderate, and weak’ in **Table 5**) of the changes, emphasizing its predictive ability. For example, Zhong et al. [79] reported that incorporating Al into Mg-based storage alloys resulted in a reduction in the dehydrating enthalpy and an increase in plateau pressures. According to the work, the reaction enthalpy of the Mg_{0.95}Al_{0.05} alloy is measured as −72.1 kJ/mol H₂, where the stability of hydride is decreased compared to that of pure Mg (−77.9 kJ/mol H₂). Another result on the Mg_{0.95}In_{0.05} alloy by Zhong et al. [81] reported a more pronounced destabilizing effect of the hydride phase (−67.8 kJ/mol H₂) at the same solute composition. These results demonstrate that the presence of In atoms has a greater destabilizing effect than the presence of Al atoms. As illustrated in **Fig. 3**, the present DFT calculation well reproduce this trend (i.e., −47.27 kJ/mol H₂ for Mg₃₁Al₁H₆₄ and −42.92 kJ/mol H₂ for Mg₃₁In₁H₆₄).

Another aspect that should be considered in the design of hydrogen storage alloys is the volume change caused by the hydrogenation reaction (i.e., dilatation). When hydrogen storage alloys transform into hydrides under hydrogen charging conditions, they usually undergo dilatation. Such dilatation results in significant internal stress that can ultimately lead to the fracture of materials, which is beneficial for the initial activation caused by the exposure of the native surface without oxides. Nevertheless, a greater dilatation is generally not preferred when considering the practical applications of hydrogen storage alloys because dilatation restricts the initial filling density of the hydrogen storage alloy in the container [88]. Consequently, a hydrogen storage alloy with low dilatation is preferred to enhance its economic feasibility. The dilation owing to the hydrogenation reaction was calculated using the following equation:

$$\Delta V = \frac{V_h - V_m}{V_m}, \quad (5)$$

where V_m and V_h are the volumes of the hydrogen storage alloy and hydride, respectively. These values at 0 K were readily obtained by the DFT calculations. **Fig. 4** presents the results of dilatation due to the hydrogenation reaction involving MgH₂ hydrides. The calculated values of 31.8 % for α -MgH₂ and 29.39 % for γ -MgH₂ are in fairly good agreement with experimentally reported volume changes of 31.4 % for α -MgH₂ and 29.1 % for γ -MgH₂ [59,89]. As illustrated in **Fig. 4**, both α -MgH₂ and γ -MgH₂ exhibit a clear decrease in the dilation when alkali metals (K, Rb, Cs) and alka-

Table 5

Impact of solute elements on the stability of the $\alpha\text{-MgH}_2$ hydride predicted by the present DFT calculations compared to the reported experimental trends. The magnitude of decrease in hydrogen plateau pressure is roughly indicated as “Strong,” “Moderate,” and “Weak.” The present prediction on the stability of the hydride is taken from Table 4 and Fig. 3.

Element	Experiment			Present prediction	
	Compared alloy		Stability of hydrides	Ref.	Stability of hydride
Al	Mg _{0.95} Al _{0.05}		Destabilized (Moderate)	[79]	Destabilized (Moderate)
Al	Mg _{0.9} Al _{0.1}		Destabilized (Moderate)	[79]	Destabilized (Moderate)
Cd	Mg _{0.95} Cd _{0.05}		Destabilized (Moderate)	[80]	Destabilized (Moderate)
In	Mg _{0.95} In _{0.05}		Destabilized (Strong)	[81,82]	Destabilized (Strong)
In	Mg _{0.9} In _{0.1}		Destabilized (Strong)	[83]	Destabilized (Strong)
Ni	Mg _{0.99} Ni _{0.01}		Destabilized (Moderate)	[84]	Destabilized (Moderate)
Ni	Mg _{0.95} Ni _{0.05}		Destabilized (Moderate)	[84]	Destabilized (Moderate)
Sn	Mg _{0.95} Sn ₃ Zn ₂		Destabilized (Strong)	[85]	Destabilized (Strong)
Ti	Mg _{0.75} Ti _{0.25}		Destabilized (Moderate)	[86]	Destabilized (Moderate)
Zn	Mg _{0.97} Zn _{0.03}		Destabilized (Weak)	[87]	Destabilized (Weak)



Fig. 4. Visualization of the impact of additional alloy elements on the volume change (ΔV) due to the hydrogenation reaction, as defined in Eq. (5). Results of substitution in (a) $\alpha\text{-MgH}_2$ and (b) $\gamma\text{-MgH}_2$ hydrides are presented.

line earth elements (Ca, Sr, Ba) are presented. However, it is important to consider other important characteristics, such as changes in the reaction energy (Fig. 3) and the solubility limit of the alloying elements in Mg. The present study

provides only qualitative information, and a comprehensive review of the characteristics of each alloying element is required for the proper design of Mg-based hydrogen storage alloys.

3.2. Analysis of solute element sublattice site preference in Mg₂Ni based on DFT calculations

We now examine the role of the solute elements in Mg₂Ni-based hydrogen storage alloys. It is worth examining the detailed site preference of each alloying element first because it can significantly affect the overall performance of Mg₂Ni-based hydrogen storage alloys. We examined the site preference by considering possible off-stoichiometric compositions, as well as the stoichiometric composition (*i.e.*, Mg:Ni = 2:1). First, the site preference of each alloying element when present in the exact Mg₂Ni stoichiometric compound was calculated based on the concept of standard defect formation energy [90].

$$E_{X \rightarrow Mg\text{ site}} = [E(Mg_{47}X_1Ni_{24}) + E_{Mg}] - [E(Mg_{48}Ni_{24}) + E_X] \quad (6)$$

$$E_{X \rightarrow Ni\text{ site}} = [E(Mg_{48}Ni_{23}X_1) + E_{Ni}] - [E(Mg_{48}Ni_{24}) + E_X] \quad (7)$$

Here, $E(Mg_{48}Ni_{24})$ is the energy of the superlattice without substitution. $E(Mg_{47}X_1Ni_{24})$ and $E(Mg_{48}Ni_{23}X_1)$ represent the energy values when the solute element (X) is present at the Mg and Ni sites, respectively. The energy values obtained using Eqs. (6) and (7) were compared to determine the relative stabilities of the solute elements (X) at both sites using the following equation:

$$E_{Mg\text{ site} \rightarrow Ni\text{ site}} = E_{X \rightarrow Ni\text{ site}} - E_{X \rightarrow Mg\text{ site}} \quad (8)$$

A positive sign of $E_{Mg\text{ site} \rightarrow Ni\text{ site}}$ suggests that the solute element (X) prefers the Mg site over the Ni site, and *vice versa*.

Although predictions using standard defect formation energies provide valid information regarding the site preferences of solute elements in intermetallic compounds, this method has a limitation in that the tendency changes depending on the arbitrary choice of the reference states of pure Mg and Ni. Moreover, this method is valid only for the prediction of stoichiometric compositions. If the composition of the compound phase deviates from the Mg₂Ni stoichiometric composition (*i.e.*, Mg- or Ni-rich compositions), the examined site preferences may differ depending on the composition. If the composition deviates from the Mg₂Ni stoichiometric composition, antisite defects or vacancies must be present in the compound, and these defects can affect the site preference of each alloying element.

Therefore, we additionally performed the investigation of the site preference based on an alternative method that considers off-stoichiometric compositions. We considered off-stoichiometric compounds with only antisite defects, rather than vacancies because we expect the number of vacancies in the Mg₂Ni-based hydrogen storage alloy to be very small compared to the number of antisite defects at the usual operating temperature, which is far below its melting point. Predictions for the Mg- and Ni-rich alloys were individually made

using Eqs. (9) and (10), respectively.

$$\begin{aligned} E_{Mg\text{ site} \rightarrow Ni\text{ site}}^{(Mg\text{-rich})} &= E[(Mg_{48}), (Ni_{23}X_1)] \\ &\quad - E[(Mg_{47}X_1), (Ni_{23}Mg_1)] \end{aligned} \quad (9)$$

$$\begin{aligned} E_{Mg\text{ site} \rightarrow Ni\text{ site}}^{(Ni\text{-rich})} &= E[(Mg_{47}Ni_1), (Ni_{23}X_1)] \\ &\quad - E[(Mg_{47}X_1), (Ni_{24})] \end{aligned} \quad (10)$$

In Eq. (9), $E[(Mg_{48}), (Ni_{23}X_1)]$ represents the energy of a Mg-rich supercell with a solute X atom at the Ni site. $E[(Mg_{47}X_1), (Ni_{23}Mg_1)]$ represents the energy of a Mg-rich supercell with a solute X atom at the Mg site and an antisite Mg atom at the Ni site. As these two energy values were calculated based on supercells with exactly the same composition, there was no ambiguity in the predictions related to the arbitrary choice of reference states. Eq. (10) can be defined similarly. The calculated results for the Mg- and Ni-rich alloys are shown in Figs. 5(c and d), respectively, and the predicted site preferences are listed in Table 6. Fig. 5(d) indicates that all the solute elements exhibited a preference for Mg sites in the Ni-rich compounds. This implies that the Ni antisite defect present at the Mg site is highly unstable and that the solute atom replacing the Ni antisite defect can lower the overall energy value.

By calculating the site preference of alloys with off-stoichiometric Mg- and Ni-rich compositions, we suggest an alternative criterion for predicting stoichiometric Mg₂Ni compounds. By averaging the values obtained from Eqs. (9) and (10), the site preferences of stoichiometric compounds can be predicted.

$$E_{Mg\text{ site} \rightarrow Ni\text{ site}}^{Average} = \left(E_{Ti\text{ site} \rightarrow Mn\text{ site}}^{(Mg\text{-rich})} + E_{Ti\text{ site} \rightarrow Mn\text{ site}}^{(Ni\text{-rich})} \right) / 2 \quad (11)$$

The prediction of the site preference obtained using Eq. (11) is more advantageous than Eq. (8) because it is independent of the selection of reference states for pure Mg and Ni. The site preferences of stoichiometric compounds predicted using Eq. (8) and the results predicted using Eq. (11) are compared in Fig. 5(a and b), respectively. The predictions of the stoichiometric compounds based on both methods exhibited similar trends, whereas certain elements (As, Ge, Mn, Si, and Zn) exhibited a mismatch in sign. However, the absolute values for these elements are relatively small, which indicates the possibility that these elements can be present at both Mg and Ni sites without a clear site preference.

The calculated predictions of the off-stoichiometric compounds presented in Table 6 and Figs. 5(c and d) indicate the following tendency: if a Mg-rich base compound is considered, an additional solute element favors the Ni site rather than the Mg site, and *vice versa*. This is because the Mg-rich compound already contains Mg antisite defects in the Ni sublattice. If a solute element is added to this Mg-rich compound, there are two choices of substitution: the placement of a solute atom substituting a Mg atom at the Mg sublattice or the placement of a solute atom substituting an

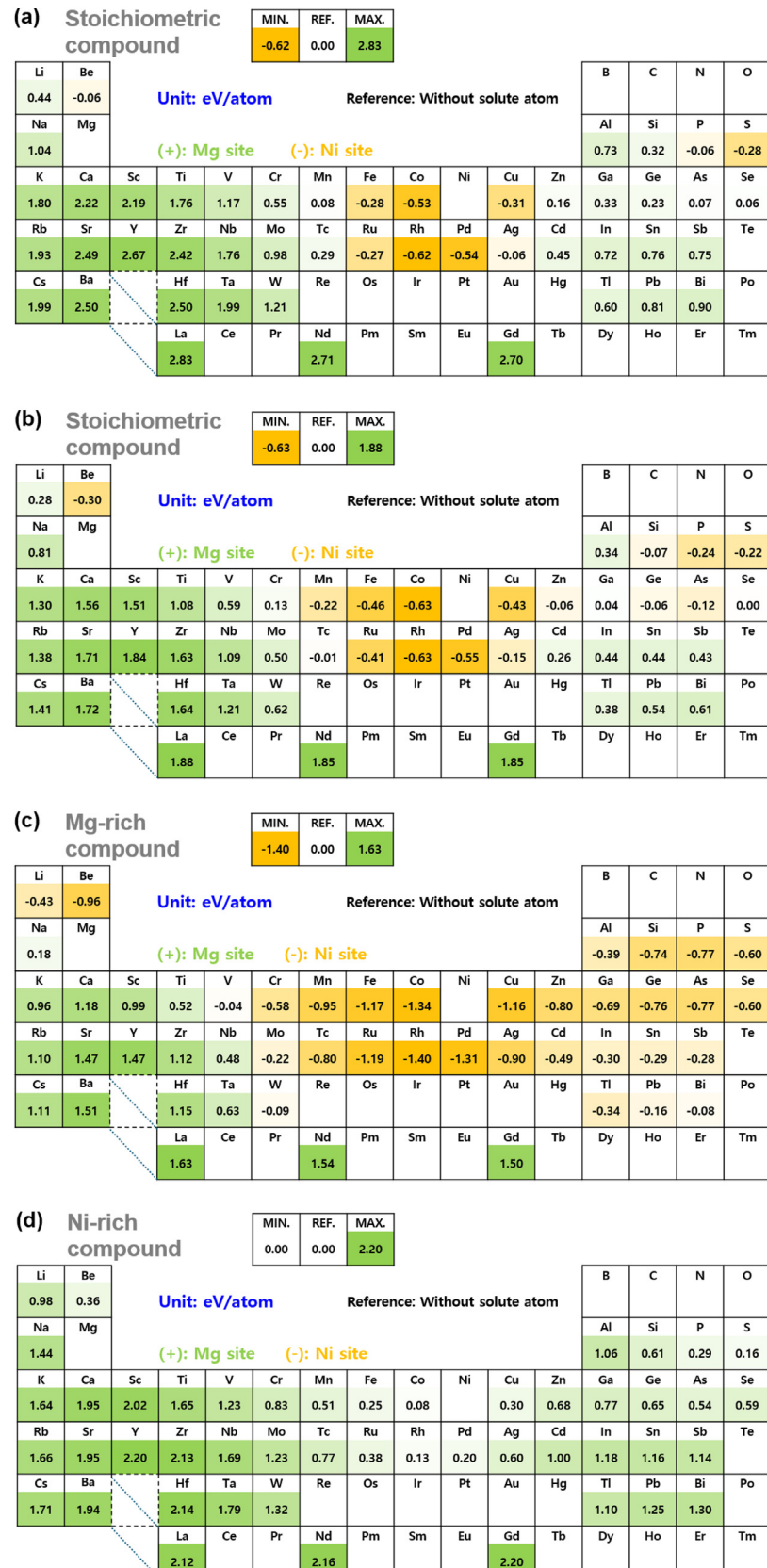


Fig. 5. Visualization of the predicted site preference of alloying elements in the Mg_2Ni compound. Predictions for (a) stoichiometric compound by Eq. (8), (b) stoichiometric compound by Eq. (11), (c) Mg-rich compound by Eq. (9), and (d) Ni-rich compound by Eq. (10) are presented.

Table 6

Site preferences of additional alloying elements in the Mg_2Ni compound predicted by the standard defect formation energy (Eqs. (6)–(8)) and the defect formation energy based on the off-stoichiometric compounds (Eqs. (9)–(11)). The preferences of each element are presented considering the stoichiometric Mg_2Ni , Mg-rich, and Ni-rich compositions.

Element	Standard defect formation energy (eV)	Defect formation energy based on off-stoichiometric compounds (eV)			Site preference		
		$E_{Mg \text{ site} \rightarrow Ni \text{ site}}^{\text{Average}}$ (Eq. (8))	$E_{Mg \text{ site} \rightarrow Ni \text{ site}}^{\text{(Eq. (11))}}$	$E_{Mg \text{ site} \rightarrow Ni \text{ site}}^{\text{(Mg-rich)}}$ (Eq. (9))	$E_{Mg \text{ site} \rightarrow Ni \text{ site}}^{\text{(Ni-rich)}}$ (Eq. (10))	Stoichiometric alloy (Eq. (11))	Mg-rich alloy (Eq. (9))
Ag	-0.063	-0.151	-0.9	0.599	Ni site	Ni site	Mg site
Al	0.731	0.339	-0.386	1.064	Mg site	Ni site	Mg site
As	0.075	-0.119	-0.774	0.536	Ni site	Ni site	Mg site
Ba	2.503	1.722	1.505	1.939	Mg site	Mg site	Mg site
Be	-0.057	-0.303	-0.96	0.355	Ni site	Ni site	Mg site
Bi	0.897	0.614	-0.076	1.303	Ni site	Ni site	Mg site
Ca	2.219	1.563	1.176	1.949	Mg site	Mg site	Mg site
Cd	0.447	0.258	-0.488	1.004	Mg site	Ni site	Mg site
Co	-0.531	-0.634	-1.343	0.076	Ni site	Ni site	Mg site
Cr	0.551	0.129	-0.576	0.834	Mg site	Ni site	Mg site
Cs	1.991	1.408	1.105	1.711	Mg site	Mg site	Mg site
Cu	-0.308	-0.43	-1.161	0.301	Ni site	Ni site	Mg site
Fe	-0.278	-0.462	-1.174	0.251	Ni site	Ni site	Mg site
Ga	0.325	0.039	-0.69	0.767	Mg site	Ni site	Mg site
Gd	2.698	1.848	1.499	2.197	Mg site	Mg site	Mg site
Ge	0.233	-0.057	-0.762	0.648	Ni site	Ni site	Mg site
Hf	2.497	1.645	1.148	2.141	Mg site	Mg site	Mg site
In	0.718	0.437	-0.302	1.176	Mg site	Ni site	Mg site
K	1.802	1.302	0.965	1.639	Mg site	Mg site	Mg site
La	2.83	1.877	1.633	2.12	Mg site	Mg site	Mg site
Li	0.441	0.276	-0.432	0.984	Mg site	Ni site	Mg site
Mn	0.077	-0.225	-0.955	0.506	Ni site	Ni site	Mg site
Mo	0.985	0.503	-0.221	1.227	Mg site	Ni site	Mg site
Na	1.036	0.811	0.176	1.445	Mg site	Mg site	Mg site
Nb	1.761	1.088	0.483	1.693	Mg site	Mg site	Mg site
Nd	2.711	1.854	1.544	2.163	Mg site	Mg site	Mg site
P	-0.058	-0.24	-0.774	0.294	Ni site	Ni site	Mg site
Pb	0.812	0.541	-0.164	1.245	Mg site	Ni site	Mg site
Pd	-0.543	-0.554	-1.308	0.2	Ni site	Ni site	Mg site
Rb	1.931	1.377	1.096	1.657	Mg site	Mg site	Mg site
Rh	-0.616	-0.635	-1.404	0.135	Ni site	Ni site	Mg site
Ru	-0.268	-0.406	-1.186	0.375	Ni site	Ni site	Mg site
S	-0.282	-0.218	-0.599	0.164	Ni site	Ni site	Mg site
Sb	0.755	0.431	-0.277	1.138	Mg site	Ni site	Mg site
Sc	2.19	1.506	0.988	2.024	Mg site	Mg site	Mg site
Se	0.058	-0.003	-0.599	0.593	Mg site	Ni site	Mg site
Si	0.32	-0.067	-0.743	0.609	Ni site	Ni site	Mg site
Sn	0.761	0.439	-0.287	1.165	Mg site	Ni site	Mg site
Sr	2.488	1.709	1.472	1.946	Mg site	Mg site	Mg site
Ta	1.993	1.212	0.629	1.794	Mg site	Mg site	Mg site
Tc	0.29	-0.014	-0.802	0.774	Ni site	Ni site	Mg site
Ti	1.758	1.083	0.515	1.65	Mg site	Mg site	Mg site
Tl	0.599	0.378	-0.345	1.1	Mg site	Ni site	Mg site
V	1.166	0.595	-0.037	1.226	Mg site	Ni site	Mg site
W	1.206	0.618	-0.087	1.322	Mg site	Ni site	Mg site
Y	2.673	1.838	1.475	2.201	Mg site	Mg site	Mg site
Zn	0.156	-0.061	-0.798	0.676	Ni site	Ni site	Mg site
Zr	2.418	1.626	1.12	2.131	Mg site	Mg site	Mg site

Mg antisite defect at the Ni sublattice; however, the latter type of substitution is usually preferred because the anti-site defect itself is somewhat unstable owing to its defective nature. However, this trend is not absolute, with different trends observed for each element. For example, Ba, Ca, Cs, Gd, Hf, K, La, Na, Nb, Nd, Rb, Sc, Sr, Ta, Ti, Y, and Zr

exhibit Mg site preferences regardless of the stoichiometry of the base compound. For elements with a strongly preferred Mg site, the adjustment of the bulk composition of the alloys is restricted to a Ni-rich composition to maintain a single-phase compound. In other words, the bulk composition should be adjusted in the same manner as $Mg_{(2-x)}Ti_xNi$

to maintain a single-phase hydrogen storage alloy. We expect that the adjustment of the bulk composition deviates in this manner (*i.e.*, $Mg_2Ni_{1-x}Ti_x$), resulting in the presence of unwanted secondary phases (*e.g.*, solid solutions, precipitates, or inclusions) that can reduce the total hydrogen storage capacity or the presence of hcp Mg-rich solid solutions. Previous experiments on adding Ti to Mg_2Ni alloys with bulk compositions of $Mg_{1.9}Ni_1Ti_{0.1}$ [91], $Mg_2Ni_{1-x}Ti_x$ ($x = 0.08, 0.12$, and 0.16) [42], and $Mg_2Ni_{0.7}Ti_{0.3}$ [92] have reported this predicted tendency. Among these, only the $Mg_{1.9}Ni_1Ti_{0.1}$ alloy [91] exhibited the single-phase Mg_2Ni -based compound. The $Mg_2Ni_{1-x}Ti_x$ ($x = 0.08, 0.12$, and 0.16) alloy [42] exhibited the dual phases of a solid solution and Mg_2Ni -based compound, whereas the $Mg_2Ni_{0.7}Ti_{0.3}$ alloy [92] exhibited the dual phases of Mg_3TiNi_2 and Mg_2Ni -based compounds.

3.3. Enthalpy of hydrogenation reactions for Mg_2Ni -based storage alloys

Based on our understanding of the site preferences of each alloying element, we extended our interest to the properties of the Mg_2Ni -based compound phase. The methodology previously employed for the Mg-based solid solution phase was similarly applied to the Mg_2Ni -based compound phase. Especially, DFT calculations were performed to obtain the energy (ΔE_r) changes due to the following hydrogenation reaction:

$$\Delta E_r = \frac{E(Mg_{48}Ni_{24}H_{96}) - E(Mg_{48}Ni_{24}) - 48E(H_2)}{48}, \quad (12)$$

where $E(Mg_{48}Ni_{24}H_{96})$ and $E(Mg_{48}Ni_{24})$ represent the DFT energy values of the supercells with the hydride and compound phases, respectively. To examine the effects of the solute elements, a dilute concentration of solute elements, where a single substitutional atom X is located in a supercell (*e.g.*, $Mg_{47}X_1Ni_{24}H_{96}$ and $Mg_{48}Ni_{23}X_1H_{96}$), was considered. For the Mg sites of the Mg_2NiH_4 hydride, three distinct sites (Mg1, Mg2, and Mg3, as shown in Fig. 2) were treated separately as possible substitutional sites. The obtained hydrogenation energy (ΔE_r) is presented in Table 7 and Fig. 6.

As listed in Table 3, the ΔE_r of Mg_2Ni without a solute atom was calculated to be -57.06 kJ/mol H_2 ; this value is presented in Table 7 as a reference. Several values in Table 7 are shaded gray, which indicates impractical cases according to the predicted site preference results in Fig. 5(b). These elements (*e.g.*, Ba, Ca, Cs, Gd, Hf, K, La, Na, Nb, Nd, Rb, Sc, Sr, Ta, Ti, Y, and Zr) always prefer Mg sites, regardless of stoichiometry. As shown in Fig. 6, the stability of hydrides varies significantly depending on the type of solute element and its presented site (*i.e.*, the Mg or Ni site).

The effect of solute elements on changes of the dilatation (ΔV) due to the hydrogenation reaction of Mg_2Ni alloys is also calculated and summarized in Table 7 and Fig. 7. The DFT results indicated that the Mg_2Ni compound without additional solute elements resulted in a volume expansion of 30.49 % owing to the hydrogenation reaction. This prediction is consistent with the reported experimental values of 31.9 %

[93] and 32.4 % [94], demonstrating the predictive accuracy of the DFT calculations. The data enabled the comparison of the dilatations resulting from the substitution of solute elements at different sites.

A comparison of the predictions by DFT calculations with the reported experimental trends is presented in Table 8, which illustrates the impact of various solute elements on the changes in the PCT curves of the ternary Mg_2Ni -based hydrogen storage alloys. For example, an experimental work on $Mg_{2-x}Al_xNi_1$ ($x = 0, 0.1$) by Li et al. [95] reported that adding Al destabilizes (*i.e.*, increase in plateau pressures) the hydride phase, consistent with the predicted DFT results; we can interpret this tendency as follows: (i) The $Mg_{2-x}Al_xNi_1$ composition was selected to be Ni-rich compared to the stoichiometric Mg_2Ni_1 compound. (ii) We expect the Al atoms in the Ni-rich alloy to be preferentially present at the Mg sites, as shown in Table 6. (iii) The Al atoms at the Mg sites results in the destabilization of the hydride phase (*i.e.*, increase in ΔE_r) as shown in Table 7.

As another example, we can compare the results of identifying the effect of Cu addition on alloys with a Mg-rich composition. Moreover, the predictions for Ag, Cu, Ca, Cr, Mn, Y, and Ti derived from the DFT calculations are also in general agreement with the reported experimental trends. According to an experimental study on $Mg_2Ni_{1-x}Cu_x$ ($x = 0-0.15$) alloys by Si et al. [43], adding Cu resulted in an increase in plateau pressures. Our DFT calculations predict that additional Cu atoms in the Mg-rich alloy are preferentially present at the Ni sites (Table 6), and this addition results in the destabilization of the hydride phase (Table 7), which is consistent with the experimental trend. In particular, the agreement between the experimental results and DFT predictions for the role of Ca, the only solute element showing a stabilizing effect among the elements in Table 7, emphasizes the credibility of the DFT prediction. Our DFT calculations predicted that Ca positioned at the Mg site stabilizes the hydride phase—a trend also reported in a previous experiment [97], which demonstrated that incorporating Ca in Mg_2Ni compounds, *e.g.*, $Mg_{62}Ca_5Ni_{33}$, results in the lowering of plateau pressures.

Moreover, it is interesting to note that the prediction is not only valid for the direction of changes (*i.e.*, stabilization or destabilization) but also for the magnitude of changes. For example, a previous experiment by Zhong et al. [92] reported that the increasing trend in the plateau pressures of the $Mg_2Ni_{0.7}Al_{0.3}$ alloy was greater than that of the $Mg_2Ni_{0.7}Mn_{0.3}$ alloy, and this trend was consistently observed in DFT calculations. The overall agreement between the present DFT calculations and the experimental trends demonstrates the reliability of the present predictions, and thus the present results provide useful information for adding solute elements not yet explored in previous experiments.

3.4. Electronic properties of Mg_2NiH_4 hydrides

Finally, we investigated the underlying mechanisms of the effect of solute elements on the properties of hydrogen stor-

Table 7

Effect of additional alloy elements on the hydrogenation reaction energy (ΔE_r) and volume change due to the hydrogenation reaction (ΔV) of Mg_2NiH_4 hydride defined in Eqs. (12) and (5), respectively. Predictions for the reaction energy were performed considering different sites (Ni, Mg1, Mg2, and Mg3) shown in Fig. 2. Results at impractical conditions, expected from the site preference prediction results in Fig. 5, are indicated in gray shading. The results considering the predicted site preference of the stoichiometric Mg_2Ni compound in Fig. 5(b) are emphasized in bold.

Element	Ni site		Mg1 site		Mg2 site		Mg3 site	
	ΔE_r (kJ/mol H ₂)	ΔV (%)	ΔE_r (kJ/mol H ₂)	ΔV (%)	ΔE_r (kJ/mol H ₂)	ΔV (%)	ΔE_r (kJ/mol H ₂)	ΔV (%)
Mg_2Ni	-57.06	30.49	-57.06	30.49	-57.06	30.49	-57.06	30.49
Ag	-51.484	30.761	-53.463	30.869	-53.342	31.294	-53.414	30.762
Al	-50.985	30.682	-52.945	31.019	-53.437	30.874	-52.672	31.244
As	-50.017	30.578	-51.297	30.694	-50.827	31.374	-50.583	31.058
Ba	-58.155	29.446	-59.689	30.222	-57.557	31.083	-58.422	30.687
Be	-52.516	31.217	-56.173	30.758	-55.544	31.165	-55.938	31.073
Bi	-50.188	29.492	-52.428	30.646	-51.483	31.460	-51.895	30.761
Ca	-55.355	29.809	-59.080	30.162	-58.769	30.151	-58.934	30.225
Cd	-50.929	30.453	-54.799	30.733	-54.855	31.076	-54.761	30.631
Co	-56.914	30.384	-54.579	30.872	-53.639	31.319	-55.023	30.848
Cr	-56.517	29.782	-54.841	30.007	-54.041	30.835	-55.138	30.599
Cs	-57.774	29.537	-57.670	30.648	-56.785	31.288	-56.672	31.369
Cu	-53.347	30.745	-53.815	31.095	-53.727	31.323	-53.959	30.952
Fe	-58.269	30.037	-54.842	30.387	-53.904	31.173	-55.752	30.540
Ga	-49.372	30.764	-52.952	31.079	-53.221	31.081	-52.273	31.221
Gd	-55.415	29.407	-56.695	30.076	-56.572	30.235	-56.937	30.026
Ge	-49.941	31.240	-52.440	31.269	-52.767	31.218	-51.919	31.316
Hf	-55.179	29.916	-54.420	30.155	-54.120	30.146	-55.029	29.737
In	-49.413	30.239	-53.247	30.629	-53.212	31.025	-52.764	30.810
K	-57.473	29.178	-58.243	30.091	-57.105	30.407	-57.476	30.420
La	-55.034	29.552	-56.874	30.080	-55.802	30.757	-56.502	30.469
Li	-54.552	30.511	-56.622	30.559	-56.492	30.633	-56.511	30.737
Mn	-56.983	29.813	-54.793	30.614	-54.430	30.959	-55.406	30.513
Mo	-57.113	29.679	-54.137	30.295	-53.178	30.804	-54.272	30.464
Na	-54.435	30.162	-57.027	30.366	-56.774	30.393	-56.776	30.500
Nb	-55.910	29.869	-53.969	30.317	-53.339	30.524	-54.354	30.407
Nd	-55.400	29.225	-56.819	29.920	-56.277	30.348	-56.896	30.094
P	-50.580	30.864	-52.448	31.054	-50.270	31.234	-49.971	31.388
Pb	-49.744	30.351	-54.029	30.843	-53.454	31.445	-53.614	31.219
Pd	-54.785	30.469	-52.809	31.209	-52.118	31.418	-52.966	30.843
Rb	-57.709	29.147	-58.368	30.196	-56.703	30.771	-57.341	30.611
Rh	-55.850	30.300	-53.215	31.207	-52.193	31.565	-53.579	30.967
Ru	-57.465	30.105	-53.961	30.515	-52.815	31.394	-54.913	30.772
S	-53.011	31.479	-52.962	31.067	-51.754	32.604	-51.603	32.336
Sb	-49.804	29.689	-51.140	30.866	-50.446	31.532	-50.596	30.877
Sc	-54.496	29.951	-56.285	30.318	-56.395	30.191	-56.469	29.944
Se	-51.794	31.262	-52.260	31.284	-50.057	31.877	-51.181	32.077
Si	-50.313	31.205	-51.633	31.260	-51.910	31.059	-50.705	31.452
Sn	-49.358	30.552	-52.588	30.953	-52.362	31.444	-52.101	31.223
Sr	-57.922	29.552	-59.730	29.966	-58.658	30.377	-59.145	30.302
Ta	-55.321	29.908	-53.864	30.089	-52.780	30.548	-53.922	30.306
Tc	-57.201	29.787	-53.959	30.716	-53.504	31.187	-54.535	30.527
Ti	-54.628	29.853	-54.877	30.306	-54.646	30.423	-55.277	30.427
Tl	-49.465	30.126	-53.832	30.707	-53.390	31.386	-53.314	31.015
V	-55.406	29.832	-54.593	30.103	-54.023	30.636	-55.033	30.532
W	-56.593	29.715	-53.744	30.303	-52.439	30.883	-53.875	30.342
Y	-55.384	29.471	-56.725	30.060	-56.662	30.145	-56.978	29.931
Zn	-51.192	31.339	-54.765	30.852	-54.807	30.939	-54.662	30.968
Zr	-55.585	29.450	-54.743	30.262	-54.513	30.234	-55.456	29.797

age alloys by analyzing the electronic properties of Mg_2NiH_4 hydrides. In particular, we analyzed the role of the solute elements by evaluating the density of states (DOS) and bonding characteristics using DFT calculations. Since there are a large number of solutes considered in the present study, we selected four example alloying elements considering tendencies of the site preference and ΔE_r . For elements that preferentially sub-

stitute the Mg site, Sb and Ba were selected because of their opposite tendencies to destabilize and stabilize the hydride phase, respectively. For elements that preferentially substitute the Ni sites, P and Ru were selected because of their opposite tendencies to destabilize and stabilize the hydride phase, respectively. Additionally, Na was selected as an example element that has only a marginal effect on hydride stability.

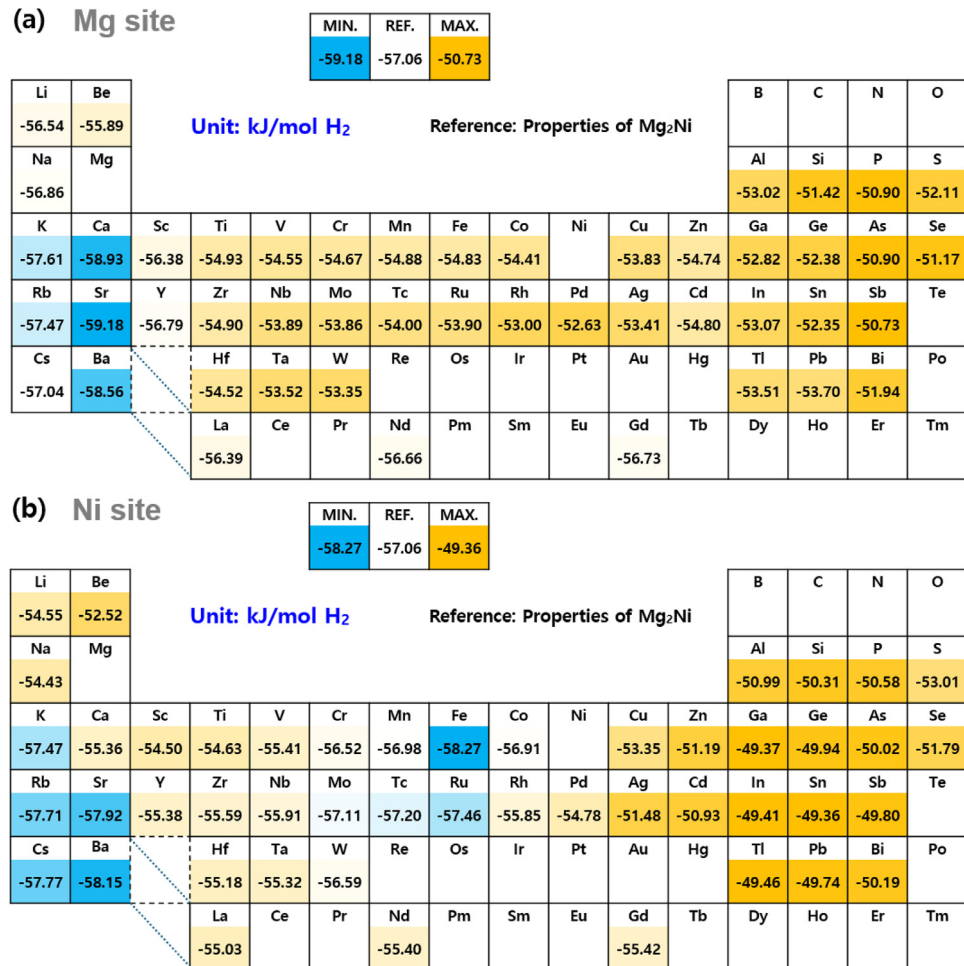


Fig. 6. Visualization of the effect of additional alloying elements on the energy of hydrogenation reaction (ΔE_r) from data listed in Table 7. Results considering a substitutional solute atom at the (a) Mg site and (b) Ni site are presented. Averaged values for different Mg sites (e.g., Mg1, Mg 2, and Mg3 in Fig. 2) are shown in (a).

Table 8

Impact of solute elements on the stability of Mg_2Ni hydrides predicted by the present DFT calculations compared to the reported experimental data. The trends of decrease and increase in hydrogen plateau pressures are indicated as “Stabilized” and “Destabilized,” respectively. Roughly summarized trends in the stability of the hydride (Table 7) considering the predicted site preferences (Table 6) are presented.

Element	Experiment				Present prediction		
	Base alloy	Compared alloy	Stability of hydrides		Ref.	Site preference	Stability of hydride
Al	Mg_2Ni	$Mg_{1.9}Al_{0.1}Ni$	Destabilized (Strong)		[95]	Mg site	Destabilized (Strong)
Al	Mg_2Ni	$Mg_{2}Ni_{0.7}Al_{0.3}$	Destabilized (Strong)		[92]	Mg site	Destabilized (Strong)
Ag	Mg_2Ni	$Mg_{1.95}Ag_{0.05}Ni$	Destabilized (Strong)		[96]	Ni site	Destabilized (Strong)
Ag	Mg_2Ni	$Mg_{1.9}Ag_{0.1}Ni$	Destabilized (Strong)		[96]	Ni site	Destabilized (Strong)
Ca	$Mg_{67}Ni_{33}$	$Mg_{62}Ca_5Ni_{33}$	Stabilized (Strong)		[97]	Mg site	Stabilized (Strong)
Cr	Mg_2Ni	$Mg_2Ni_{0.8}Cr_{0.2}$	Destabilized (Moderate)		[98]	Mg site	Destabilized (Moderate)
Cu	Mg_2Ni	$Mg_2Ni_{0.9}Cu_{0.1}$	Destabilized (Moderate)		[43]	Ni site	Destabilized (Strong)
Cu	Mg_2Ni	$Mg_2Ni_{0.8}Cu_{0.2}$	Destabilized (Moderate)		[99]	Ni site	Destabilized (Strong)
Mn	Mg_2Ni	$Mg_2Ni_{0.8}Mn_{0.2}$	Destabilized (Weak)		[98]	Ni site	Destabilized (Weak)
Mn	Mg_2Ni	$Mg_2Ni_{0.7}Mn_{0.3}$	Destabilized (Weak)		[92]	Ni site	Destabilized (Weak)
Ti	Mg_2Ni	$Mg_2Ni_{0.88}Ti_{0.12}$	Destabilized (Moderate)		[42]	Mg site	Destabilized (Moderate)
Ti	Mg_2Ni	$Mg_{1.9}Ni_1Ti_{0.1}$	Destabilized (Moderate)		[91]	Mg site	Destabilized (Moderate)
Ti	Mg_2Ni	$Mg_2Ni_{0.7}Ti_{0.3}$	Destabilized (Weak)		[92]	Mg site	Destabilized (Moderate)
Y	$Mg_{67}Ni_{33}$	$Mg_{67}Ni_{30}Y_3$	Destabilized (Moderate)		[94]	Mg site	Destabilized (Weak)
Zn	Mg_2Ni	$Mg_2Ni_{0.83}Zn_{0.17}$	Destabilized (Strong)		[100]	Ni site	Destabilized (Strong)
Zn	Mg_2Ni	$Mg_2Ni_{0.83}Zn_{0.17}$	Destabilized (Strong)		[100]	Ni site	Destabilized (Strong)
Zr	Mg_2Ni	$Mg_2Ni_{0.9}Zr_{0.1}$	Destabilized (Weak)		[101]	Mg site	Destabilized (Weak)

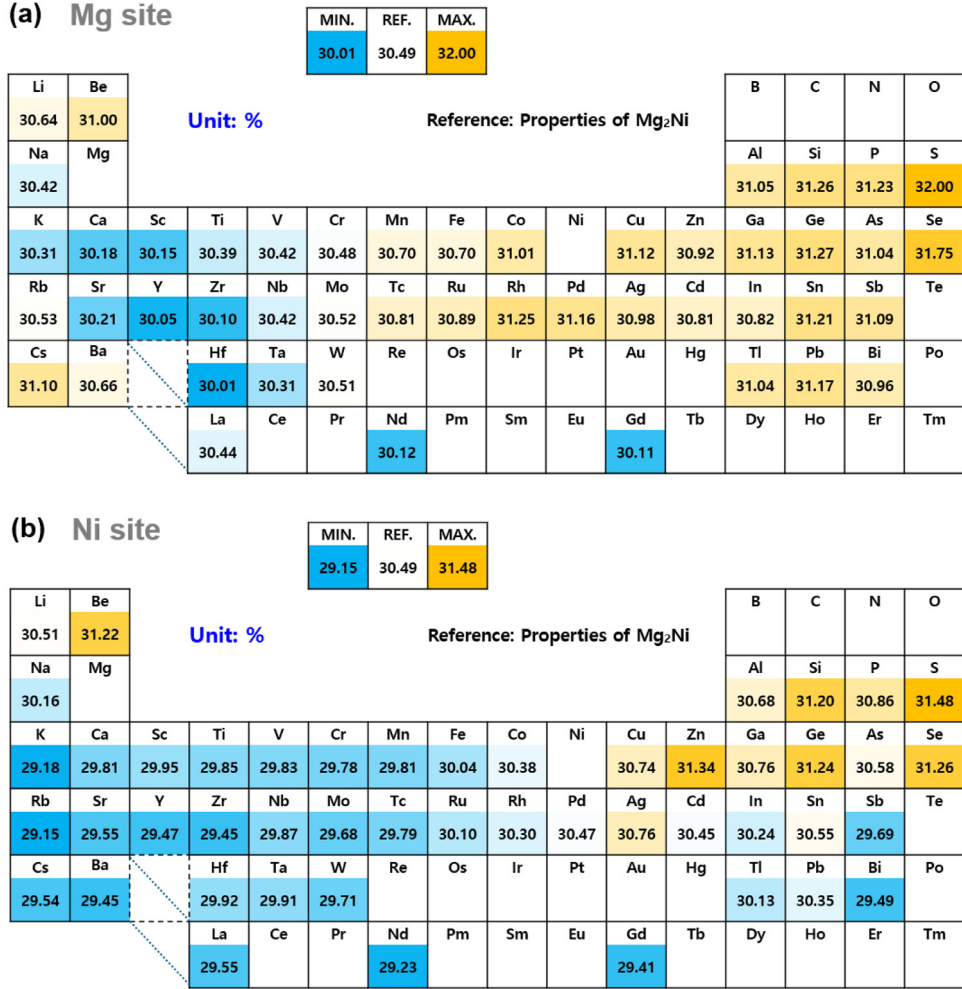


Fig. 7. Visualization of the impact of additional solute elements on the volume change due to the hydrogenation reaction (ΔV) of Mg₂Ni alloys from data listed in Table 7. Results considering a substitutional solute atom at the (a) Mg site and (b) Ni site are presented. Averaged values for different Mg sites (e.g., Mg1, Mg 2, and Mg3 in Fig. 2) are shown in (a).

Fig. 8 shows the examined DOS of the hydrides without (e.g., Mg₄₈Ni₂₄H₉₆) and with (e.g., Mg₄₇X₁Ni₂₄H₉₆ and Mg₄₈Ni₂₃X₁H₉₆) solute atom X. The total density of states (TDOS) and partial density of states (PDOS) are shown separately displayed in the figure. These analyses were conducted to analyze the electronic structure and gain insight into the detailed mechanisms of the influence of the solute elements. Fig. 8(a) shows the TDOS of Mg₄₈Ni₂₄H₉₆ and the partial density of states (PDOS) of the constituent elements (i.e., Mg, Ni, and H), which enable a comprehensive understanding of the electronic structure of the Mg₂NiH₄ hydride. Examination of the TDOS reveals a bandgap of approximately 1.53 eV between the valence and conduction bands, exhibiting the characteristics of a semiconductor. The TDOS peak in a range between the energy of -2.5 eV and the Fermi energy (E_f) is predominantly characterized by the Ni *d* orbital. This range is also characterized by superposition with Mg orbitals, whereas the overall DOS values are small. PDOS analysis reveals that the Ni *d* orbital is the primary contributor to the electronic states near the Fermi level and plays

a significant role in bonding with hydrogen atoms. The Ni *d* orbitals have a higher spatial overlap with the H *s* orbitals, allowing for stronger hybridization and more effective electron sharing between the Ni and H atoms. This results in a deeper potential well and stronger binding between Ni and H atoms. Conversely, the Mg atoms primarily contribute through *s* and *p* orbitals, which have less directional overlap with the H *s* orbitals, resulting in weaker bonding interactions. The difference in bonding strength between Ni-H and Mg-H is crucial to the thermodynamic stability of Mg₂NiH₄ hydride, with the stronger Ni-H bonds playing a significant role in enhancing the hydride's overall stability. This finding is in accordance with previous DFT results [102,103].

Fig. 8(c and d) illustrate the DOS of the hydrides with P and Sb atoms at the Ni and Mg3 sites, respectively, which exhibit a destabilization trend of the hydrides. Fig. 8(e and f) illustrate the DOS of the hydrides with Ru and Ba atoms at the Ni and Mg3 sites, respectively, which exhibit a stabilization trend of the hydrides. Upon the substitution of Mg with Sb (Fig. 8(d)), a transition to metallic behavior is observed,

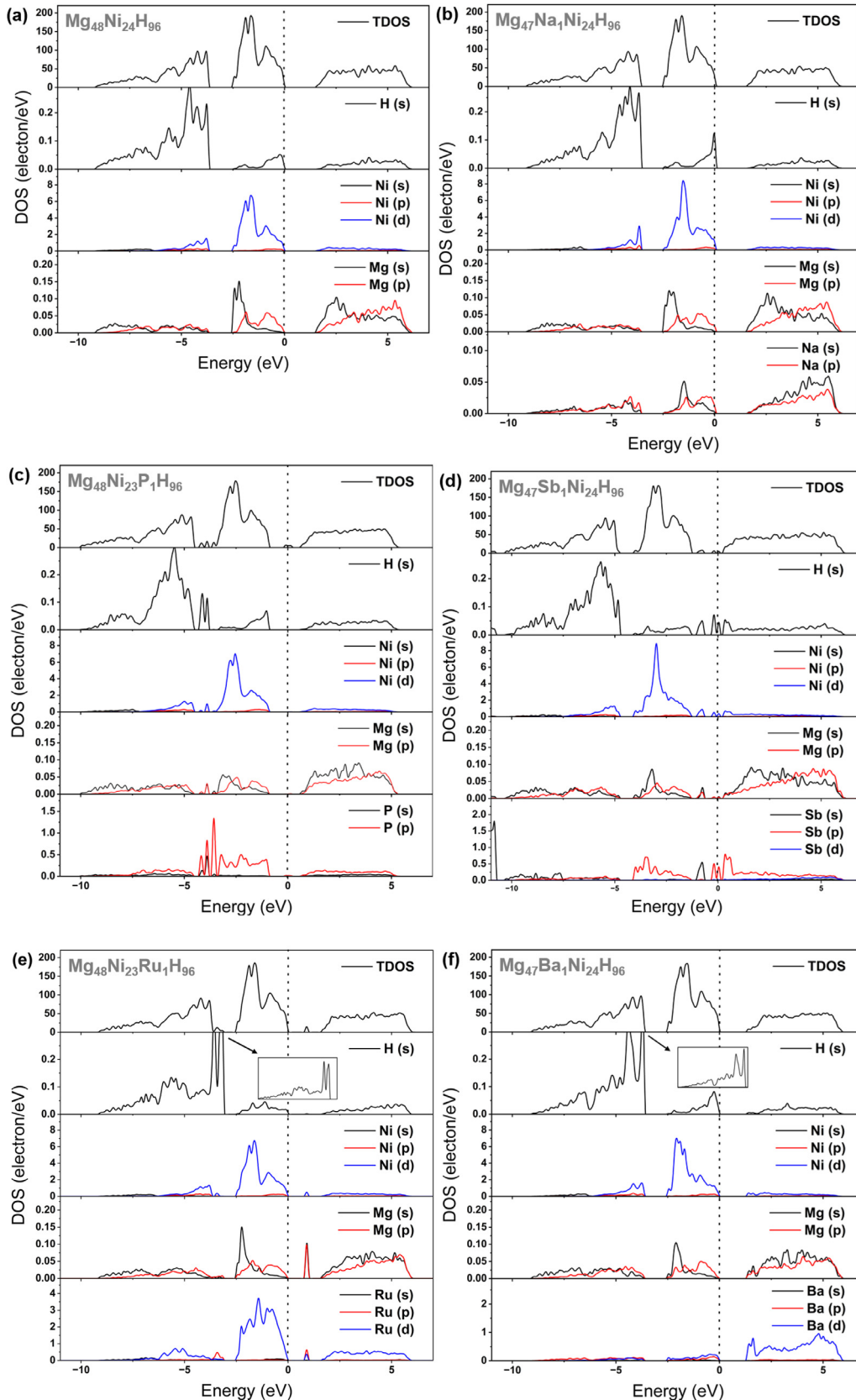


Fig. 8. Total density of states (TDOS) and partial density of states (PDOS) of the (a) $\text{Mg}_{48}\text{Ni}_{24}\text{H}_{96}$, (b) $\text{Mg}_{47}\text{Na}_1\text{Ni}_{24}\text{H}_{96}$, (c) $\text{Mg}_{48}\text{Ni}_{23}\text{P}_1\text{H}_{96}$, (d) $\text{Mg}_{47}\text{Sb}_1\text{Ni}_{24}\text{H}_{96}$, (e) $\text{Mg}_{48}\text{Ni}_{23}\text{Ru}_1\text{H}_{96}$, and (f) $\text{Mg}_{47}\text{Ba}_1\text{Ni}_{24}\text{H}_{96}$. A solute atom is presented at the Mg3 site for (b, d, f), while a solute atom is presented at the Ni site for (c, e). The energy of the Fermi level (E_f) is set to zero and indicated by a dashed line.

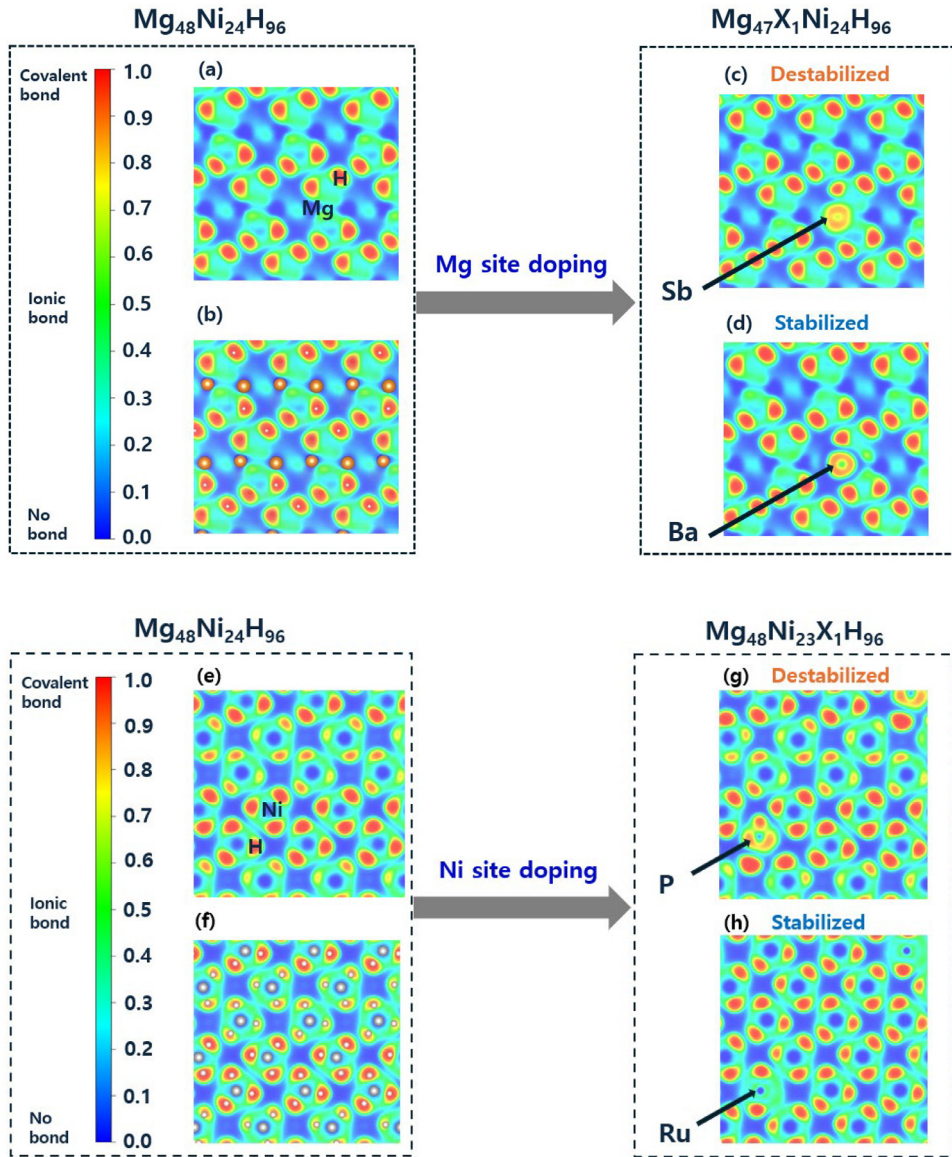


Fig. 9. Electron localization function (ELF) plots are illustrated on selected cross-sections of the hydride structure. (a, b) and (e, f) Plots of the $\text{Mg}_{48}\text{Ni}_{24}\text{H}_{96}$ hydride considering different cross-sectional positions to focus on the positions of Mg and Ni atoms, respectively. (b, f) Additional plots with atomic positions. (c) $\text{Mg}_{47}\text{Sb}_1\text{Ni}_{24}\text{H}_{96}$ and (d) $\text{Mg}_{47}\text{Ba}_1\text{Ni}_{24}\text{H}_{96}$ represent plots of the hydrides where a solute atom is presented at the Mg₃ site. (g) $\text{Mg}_{48}\text{Ni}_{23}\text{P}_1\text{H}_{96}$ and (h) $\text{Mg}_{48}\text{Ni}_{23}\text{Ru}_1\text{H}_{96}$ represent plots of the hydrides where a solute atom is presented at the Ni site.

characterized by the collapse of the band gap and the appearance of states at the Fermi level. Moreover, the TDOS reveals an increase in the density of states at higher energy levels, particularly above the Fermi level, where the Sb p orbitals introduce additional states that contribute to the destabilization of the system. This destabilization is linked to an increase in the DOS at elevated energy states, which enhances the electronic excitability and reduces the energy required for electron transitions, thereby facilitating a less stable electronic environment. The increase in high-energy DOS reflects the introduction of less-bound electronic states available for thermal excitation and contributes to the overall instability of the hydride. The presence of Sb atoms disrupts the original Ni-H bonding network by introducing localized electronic states

that interfere with the cohesive forces between hydrogen and the neighboring metal atoms. These additional states create electron localization around Sb, weaken the Ni-H and Mg-H interactions, and render the system more prone to electronic fluctuations and instability. The overall effect is to significantly reduce the stability of the hydrides, which aligns with the goal of enhancing hydrogen release during the desorption process.

In contrast, the substitution of Mg with Ba (Fig. 8(f)) maintains the semiconducting nature of the Mg_2NiH_4 hydride, with only a slight reduction in the band gap, preserving a relatively stable electronic structure. The PDOS shows that the Ba d orbitals enhance bonding interactions with hydrogen, as evidenced by the increased contributions of Ba states be-

low the Fermi level. This result indicates that the H atom contributes significantly to the valence electrons, suggesting that the bonding interaction between H and the nearby metal atoms is strengthened. In general, the greater the number of bonding electrons, the stronger the charge interaction, which increases the structural stability of the system [104]. This suggests that although the Ba atom introduces some electronic modifications, it predominantly reinforces the existing metal-H bonding framework rather than destabilizing it.

The supporting observations from Fig. 8(b, c and e) provide further insights into the contrasting effects of the solute elements. Na substitution induces minimal changes in the electronic structure, reflecting its limited impact on the stability of the hydride, as shown in Fig. 8(b). In contrast, P substitution slightly reduces the band gap and introduces states near the conduction band, partially destabilizing the hydride, as shown in Fig. 8(c). As illustrated in Fig. 8(e), the Ru substitution enhances the interaction between Ru and H, leading to a localized electron density that contributes to maintaining the stability of the hydride.

Overall, the results demonstrate that solute elements such as Sb and P effectively destabilize Mg_2NiH_4 hydride by modifying the electronic landscape, particularly through the introduction of high-energy states that facilitate electronic instability. In contrast, elements such as Ba and Ru either preserve or slightly reinforce metal-H bonds, resulting in a more stable hydride phase. These findings highlight the importance of selecting the appropriate alloying elements to tailor the electronic properties of hydrides. This approach helps achieve the desired balance between the destabilization of hydrides for enhanced hydrogen desorption and the maintenance of the thermodynamic stability of hydrides for enhanced hydrogen storage capacity, which is crucial for practical applications of hydrogen storage alloys.

In the present study, the electron localization function (ELF) was examined to elucidate the effect of solute atoms on bonding characteristics. As illustrated in Fig. 9, regions with an ELF value near 1.0, represent a case where electrons are fully localized. In regions with an ELF value below 0.5, the Pauli repulsion becomes more pronounced than in a uniform electron gas, indicating that electrons are dispersed and delocalized in those regions. Fig. 9(a, b, e, and f) depict the ELF plots of the $Mg_{48}Ni_{24}H_{96}$ hydride. As illustrated in Fig. 9, red regions surrounding the H atoms, which exhibit ELF values of 0.9–1.0, indicate that the electrons are highly localized. In contrast, the blue regions at the positions of the Ni and Mg atoms indicate that the metal atoms are in the delocalization situation. Substantial ELF values between the metal and H indicate the presence of a covalent-like bond, while a certain level of ionic bonding also occurs as a result of electron donation from the metal to the H atoms. Upon examination of Fig. 9(c and g) for solute elements (Sb and P) that destabilize the hydride phase, the presence of those atoms leads to an overall shrinkage of the highly localized regions (ELF values of 0.9 – 1.0) near the H atoms. A reduction in the electron density surrounding the hydrogen atoms indicates weakening of the interaction between hydrogen and

the metal atoms. Fig. 9(d and h) illustrate a contrasting trend for the solute elements (Ba and Ru) that stabilize the hydride phase. The substitution of the Ba and Ru atoms resulted in a more localized distribution of electrons around the hydrogen atoms. These observations explain why hydrogen storage properties vary significantly depending on the individual solute elements.

4. Conclusion

First-principles DFT calculations were performed to analyze the impact of various solute elements on the performance of Mg-Mg₂Ni hydrogen storage alloys. We investigated the important characteristics of hydrogen storage alloys by considering both Mg-based solid solution and Mg₂Ni-based intermetallic compound phases, where the hydride forms are MgH₂ and Mg₂NiH₄, respectively. In particular, qualitatively valid information for predicting changes in plateau pressures in the PCT curve was provided by calculating changes in the energy of related hydrogenation reactions. The effects of alloying elements on volume changes due to hydrogenation reactions were also obtained to provide additional criteria for the practical use of hydrogen storage alloys. For the Mg-Ni-based intermetallic compound, we examined the site preference of each alloying element, considering the designated stoichiometry of the base alloy. Based on the revealed site preferences, the effects of various possible alloying elements on the properties of Mg₂Ni-based hydrides were also examined. Electronic structure analyses were further conducted to elucidate the detailed mechanisms underlying the role of the additional solute elements. The results of this study provide meaningful data for designing Mg-Mg₂Ni-based hydrogen storage alloys.

Declaration of competing interest

The authors declare that they have no known competing financial interests or personal relationships that could have appeared to influence the work reported in this paper.

CRediT authorship contribution statement

Min-Seok Yoon: Writing – review & editing, Writing – original draft, Visualization, Validation, Software, Methodology, Investigation, Formal analysis, Data curation. **Jae Hur:** Visualization, Validation, Methodology. **Seo-Hui Park:** Visualization, Validation, Methodology. **Ui-Jong Lee:** Visualization, Validation, Methodology. **Guanglong Xu:** Writing – review & editing, Validation, Methodology. **Hyung-Ki Park:** Methodology, Data curation, Conceptualization. **Byeong-Chan Suh:** Writing – review & editing, Writing – original draft, Resources, Project administration, Conceptualization. **Young Min Kim:** Writing – review & editing, Writing – original draft, Resources, Project administration, Conceptualization. **Won-Seok Ko:** Writing – review & editing, Writing – original draft, Supervision, Project administration, Funding acquisition, Conceptualization.

Acknowledgments

This research was supported by the National Research Foundation of Korea (NRF) funded by the Ministry of Science and ICT (Grant No. NRF-2022M3D1A2095313). This research was also supported by the National Research Council of Science & Technology (NST) grant by the Korea government (MSIT) (No. GTL24051-300). This research was also supported by the Ministry of Trade, Industry and Energy through machinery and equipment industry technology development project (Grant No. 20018661). H.-K.P acknowledges support from the Korea Institute of Industrial Technology (KITECH EH - 24 - 0007). W.-S.K acknowledges support from the National Supercomputing Center with supercomputing resources including technical support (KSC-2021-CRE-0402).

Data availability

Data supporting the findings of this study are available from the corresponding author (wonsko@inha.ac.kr) upon request.

References

- [1] X. Li, Z. Yuan, C. Liu, Y. Sui, T. Zhai, Z. Hou, Z. Han, Y. Zhang, Int J Hydro Energy 50 (2024) 1401–1417.
- [2] T.R. Somo, M.V. Lototskyy, V.A. Yartys, M.W. Davids, S.N. Nyamsi, J Energy Storage 73 (2023) 108969.
- [3] B. Sakintuna, F. Lamari-Darkrim, M. Hirscher, Int J Hydro Energy 32 (9) (2007) 1121–1140.
- [4] T. Matsunaga, F. Buchter, P. Mauron, M. Bielman, Y. Nakamori, S. Orimo, N. Ohba, K. Miwa, S. Towata, A. Züttel, J Alloys Compd 459 (1–2) (2008) 583–588.
- [5] L. George, S.K. Saxena, Int J Hydro Energy 35 (11) (2010) 5454–5470.
- [6] H. Wan, L. Ran, H. Lu, J. Qiu, H. Zhang, Y. Yang, Y.a. Chen, J. Wang, F. Pan, J Magnes Alloys (2024), doi:10.1016/j.jma.2024.01.014.
- [7] Y. Liu, M. Yue, Y. Guo, Y. Jiang, Y. Sun, L. Feng, Y. Wang, J Magnes Alloys (2024), doi:10.1016/j.jma.2024.04.031.
- [8] Q. Li, Y. Lu, Q. Luo, X. Yang, Y. Yang, J. Tan, Z. Dong, J. Dang, J. Li, Y. Chen, B. Jiang, S. Sun, F. Pan, J Magnes Alloys 9 (6) (2021) 1922–1941.
- [9] Z. Ma, J. Zou, D. Khan, W. Zhu, C. Hu, X. Zeng, W. Ding, J Mater Sci Technol 35 (10) (2019) 2132–2143.
- [10] A. Andreasen, Int J Hydrogen Energy 33 (24) (2008) 7489–7497.
- [11] J. Zhang, Y.N. Huang, P. Peng, C. Mao, Y.M. Shao, D.W. Zhou, Int J Hydro Energy 36 (9) (2011) 5375–5382.
- [12] P.V. Jasen, E.A. González, G. Brizuela, O.A. Nagel, G.A. González, A. Juan, Int J Hydro Energy 32 (18) (2007) 4943–4948.
- [13] M.J. van Setten, G.A. de Wijs, G. Brocks, Phys Rev B 76 (7) (2007) 075125.
- [14] S. Shen, W. Liao, Z. Cao, J. Liu, H. Wang, L. Ouyang, J Mater Sci Technol 178 (2024) 90–99.
- [15] J. Garcia-Navarro, M.A. Isaacs, M. Favaro, D. Ren, W.J. Ong, M. Grätzel, P. Jiménez-Calvo, Global Chall 8 (6) (2024) 2300073.
- [16] H. Zhong, L.Z. Ouyang, J.S. Ye, J.W. Liu, H. Wang, X.D. Yao, M. Zhu, Energy Storage Mater 7 (2017) 222–228.
- [17] F. Mirshafiee, M. Rezaei, Int J Hydro Energy 48 (83) (2023) 32356–32370.
- [18] Y. Zhu, L. Ouyang, H. Zhong, J. Liu, H. Wang, H. Shao, Z. Huang, M. Zhu, Angew Chem 132 (22) (2020) 8701–8707.
- [19] L. Ouyang, W. Chen, J. Liu, M. Felderhoff, H. Wang, M. Zhu, Adv Energy Mater 7 (19) (2017) 1700299.
- [20] T. Káňa, J. Čermák, L. Král, Int J Hydro Energy 46 (29) (2021) 15691–15701.
- [21] H. Zhang, S. Shang, J.E. Saal, A. Saengdeejing, Y. Wang, L.-Q. Chen, Z.-K. Liu, Intermetallics 17 (11) (2009) 878–885.
- [22] L.W. Huang, O. Elkedi, R. Hamzaoui, J Alloys Compd 509 (2011) S328–S333.
- [23] H. Sun, X. Gao, F. Zhao, Y. Li, Y. Zhang, H. Ren, Int J Hydro Energy 45 (53) (2020) 28974–28984.
- [24] Y. Li, G. Sun, Y. Mi, Am J Anal Chem 7 (1) (2016) 67–74.
- [25] Y. Zeng, K. Fan, X. Li, B. Xu, X. Gao, L. Meng, Int J Hydro Energy 35 (19) (2010) 10349–10358.
- [26] T. Kelkar, S. Pal, J Mater Chem 19 (25) (2009) 4348–4355.
- [27] T. Hussain, T.A. Maark, S. Chakraborty, R. Ahuja, Chemphyschem 16 (12) (2015) 2557–2561.
- [28] Z. Han, Y. Wu, H. Yu, S. Zhou, J Magnes Alloys 10 (6) (2022) 1617–1630.
- [29] B. Li, X. Peng, Y. Yang, G. Wei, Q. Li, Y.a. Chen, F. Pan, Sep Purif Technol 353 (2025).
- [30] Q. Luo, Y. Guo, B. Liu, Y. Feng, J. Zhang, Q. Li, K. Chou, J Mater Sci Technol 44 (2020) 171–190.
- [31] X. Pang, L. Ran, Y.a. Chen, Y. Luo, F. Pan, J Magnes Alloys 10 (3) (2022) 821–835.
- [32] N.A. Ali, M. Ismail, J Magnes Alloys 9 (4) (2021) 1111–1122.
- [33] Y. Jia, Y. Guo, J. Zou, X. Yao, Int J Hydro Energy 37 (9) (2012) 7579–7585.
- [34] L. Li, Z. Zhang, L. Jiao, H. Yuan, Y. Wang, Int J Hydro Energy 41 (40) (2016) 18121–18129.
- [35] S. Shen, L. Ouyang, J. Liu, H. Wang, X.-S. Yang, M. Zhu, J Magnes Alloys 11 (9) (2023) 3174–3185.
- [36] H. Wan, L. Ran, H. Lu, J. Qiu, H. Zhang, Y. Yang, J. Wang, F. Pan, J Magnes Alloys (2024), doi:10.1016/j.jma.2024.01.014.
- [37] T. Zhong, T. Xu, L. Zhang, F. Wu, Y. Jiang, X. Yu, J. Magnes. Alloys (2024), doi:10.1016/j.jma.2024.04.027.
- [38] X. Ding, R. Chen, X. Chen, H. Fang, Q. Wang, Y. Su, J. Guo, J Magnes Alloys 11 (3) (2023) 903–915.
- [39] M. Mezbahul-Islam, M. Medraj, Calphad 33 (3) (2009) 478–486.
- [40] X.Q. Tran, S.D. McDonald, Q. Gu, T. Yamamoto, K. Shigematsu, K. Aso, E. Tanaka, S. Matsumura, K. Nogita, J Power Sources 341 (2017) 130–138.
- [41] J. Čermák, L. Král, Acta Mater 56 (12) (2008) 2677–2686.
- [42] P. Wei, W. Huang, X. Ding, Y. Li, Z. Liu, T. Si, K. Wang, Q. Wang, H.-W. Li, Q. Zhang, Dalton Trans 47 (25) (2018) 8418–8426.
- [43] T. Si, Y. Ma, Y. Li, D. Liu, Mater Chem Phys 193 (2017) 1–6.
- [44] Y.H. Cho, A.K. Dahle, Mater Sci Forum 638–642 (2010) 1085–1090.
- [45] Y. Li, Q. Gu, Q. Li, T. Zhang, Scr Mater 127 (2017) 102–107.
- [46] C. Lu, Y. Ma, F. Li, H. Zhu, X. Zeng, W. Ding, T. Deng, J. Wu, J. Zou, J Mater Chem A 7 (24) (2019) 14629–14637.
- [47] Y. Qi, Z. Zhang, Q. Tang, J. Liu, R. Shi, J. Zhang, Y. Liu, J. Wang, J. Zhang, S. Chen, Y. Zhu, Chem Mater 36 (12) (2024) 6288–6298.
- [48] Y. Zhang, T. Zhai, B. Li, H. Ren, W. Bu, D. Zhao, J. Mater. Sci. Technol. 30 (10) (2014) 1020–1026.
- [49] Z. Lan, Z. Liu, H. Liang, W. Shi, R. Zhao, R. Li, Y. Fan, H. Liu, J. Guo, J Mater Sci Technol 196 (2024) 12–24.
- [50] A. Zaluska, L. Zaluski, J.O. Ström-Olsen, J Alloys Compd 289 (1) (1999) 197–206.
- [51] N.A. Niaz, I. Ahmad, W.S. Khan, S.T. Hussain, J. Mater Sci Technol 28 (5) (2012) 401–406.
- [52] X. Sun, X. Yang, Y. Lu, Q. Luo, C. Wu, Y. Zhang, T. Lyu, Q. Gu, Q. Li, F. Pan, J Mater Sci Technol 202 (2024) 119–128.
- [53] B. Liu, S. Guo, Z. Hou, C. Li, X. Mu, L. Xu, D. Zhao, J Phys Chem Solids 181 (2023) 111545.
- [54] P.E. Blochl, Phys Rev B 50 (24) (1994) 17953–17979.
- [55] G. Kresse, J. Hafner, Phys Rev B 49 (20) (1994) 14251–14269.
- [56] J.P. Perdew, K. Burke, M. Ernzerhof, Phys Rev Letters 77 (18) (1996) 3865.
- [57] H. Ding, S. Zhang, Y. Zhang, S. Huang, P. Wang, H. Tian, Int J Hydro Energy 37 (8) (2012) 6700–6713.
- [58] M. Methfessel, A.T. Paxton, Phys Rev B 40 (6) (1989) 3616–3621.

- [59] M. Bortz, B. Bertheville, G. Böttger, K. Yvon, *J Alloys Compd* 287 (1–2) (1999) L4–L6.
- [60] V. Charbonnier, K. Asano, H. Kim, K. Sakaki, *Inorg Chem* 59 (19) (2020) 14263–14274.
- [61] P. Vajeeston, P. Ravindran, B. Hauback, H. Fjellvåg, A. Kjekshus, S. Furuse, M. Hanfland, *Phys Rev B* 73 (22) (2006) 224102.
- [62] M.V. Simić, M. Zdujić, R. Dimitrijević, L. Nikolić-Bujanović, N.H. Popović, *J Power Sources* 158 (1) (2006) 730–734.
- [63] F. Cuevas, J.F. Fernández, J.R. Ares, F. Leardini, M. Latroche, *J Solid State Chem* 182 (10) (2009) 2890–2896.
- [64] G. Garcia, J. Abriata, J. Sofo, *Phys Rev B* 59 (18) (1999) 11746.
- [65] M. Liu, D. Qiu, M.-C. Zhao, G. Song, A. Atrens, *Scr Mater* 58 (5) (2008) 421–424.
- [66] N. Novaković, L. Matović, J.G. Novaković, M. Manasijević, N. Ivanović, *Mater Sci Eng B* 165 (3) (2009) 235–238.
- [67] C. Shen, K.-F. Aguey-Zinsou, *J Mater Chem A* 5 (18) (2017) 8644–8652.
- [68] J. Töpler, H. Buchner, H. Säufferer, K. Knorr, W. Prandl, *J Less-Common Met* 88 (2) (1982) 397–404.
- [69] L. Ouyang, H. Dong, C. Peng, L. Sun, M. Zhu, *Int. J Hydro Energy* 32 (16) (2007) 3929–3935.
- [70] P. Zolliker, K. Yvon, J. Jorgensen, F. Rotella, *Inorg Chem* 25 (20) (1986) 3590–3593.
- [71] J.L. Soubeyroux, D. Fruchart, A. Mikou, M. Pezat, B. Darriet, *Mater Res Bull* 19 (9) (1984) 1119–1128.
- [72] Q. Lu, Z. Shao, C. Cui, G. Yang, L. Xu, H. Yang, *Int J Hydro Energy* 48 (35) (2023) 13236–13247.
- [73] D. Vyas, P. Jain, J. Khan, V. Kulshrestha, A. Jain, I.P. Jain, *Int J Hydro Energy* 37 (4) (2012) 3755–3760.
- [74] E. van Steen, P. van Helden, *J Phys Chem C* 114 (13) (2010) 5932–5940.
- [75] M. Pozzo, D. Alfe, *Phys Rev B* 77 (10) (2008) 104103.
- [76] X. Li, Y. Qin, J. Fu, J. Zhao, *Comput Mater Sci* 98 (2015) 328–332.
- [77] T. Adit Maark, T. Hussain, R. Ahuja, *Int J Hydro Energy* 37 (11) (2012) 9112–9122.
- [78] M.A. Salam, B. Abdullah, S. Sufian, F. Karimzadeh, *J Nanomater* 2014 (1) (2014).
- [79] H.C. Zhong, H. Wang, L.Z. Ouyang, *Int. J. Hydrogen Energy* 39 (7) (2014) 3320–3326.
- [80] G. Liang, R. Schulz, *J Mater Sci* 39 (5) (2004) 1557–1562.
- [81] H.C. Zhong, H. Wang, J.W. Liu, D.L. Sun, M. Zhu, *Scr Mater* 65 (4) (2011) 285–287.
- [82] C. Zhou, Z.Z. Fang, J. Lu, X. Luo, C. Ren, P. Fan, Y. Ren, X. Zhang, *J Phys Chem C* 118 (22) (2014) 11526–11535.
- [83] C. Zhou, Z.Z. Fang, J. Lu, X. Zhang, *J Am Chem Soc* 135 (30) (2013) 10982–10985.
- [84] L.A. Bendersky, C. Chiu, V.M. Skripnyuk, E. Rabkin, *Int J Hydro Energy* 36 (9) (2011) 5388–5399.
- [85] H. Zhong, J. Xu, *Int J Hydro Energy* 44 (5) (2019) 2926–2933.
- [86] X. Yang, W. Li, J. Zhang and Q. Hou, *Materials*, **16** (4), 2023, 1587.
- [87] H.C. Zhong, Y.S. Huang, Z.Y. Du, H.J. Lin, X.J. Lu, C.Y. Cao, J.H. Chen, L.Y. Dai, *Int J Hydrogen Energy* 45 (51) (2020) 27404–27412.
- [88] M. Lototskyy, V. Linkov, *Int J Energ. Res.* 46 (15) (2022) 22049–22069.
- [89] W. Zachariasen, C. Holley, J. Stamper, *Acta Crystallogr* 16 (5) (1963) 352–353.
- [90] W.-S. Ko, K.B. Park, H.-K. Park, *J Mater Sci Technol* 92 (2021) 148–158.
- [91] G. Liang, J. Huot, S. Boily, A. Van Neste, R. Schulz, *J Alloys Compd* 282 (1) (1999) 286–290.
- [92] H.-c. Zhong, J.-b. Xu, C.-h. Jiang, X.-j. Lu, *Trans Nonferrous Met Soc China* 28 (12) (2018) 2470–2477.
- [93] F. Guo, T. Zhang, L. Shi, L. Song, *J Magnes Alloys* 11 (4) (2023) 1180–1192.
- [94] T. Zhang, W. Song, H. Kou, J. Li, *Appl Surf Sci* 371 (2016) 35–43.
- [95] Q. Li, *Int J Hydrogen Energy* 29 (13) (2004) 1383–1388.
- [96] L. Qian, L. Qin, J. Lijun, K.-C. Chou, Z. Feng, Z. Qiang, W. Xiuying, *J Alloys Compd* 359 (1–2) (2003) 128–132.
- [97] A. Takasaki, K. Sasao, *J Alloys Compd.* 404–406 (2005) 431–434.
- [98] X. Liu, S. Wu, X. Cai, L. Zhou, *Int J Hydrogen Energy* 48 (45) (2023) 17202–17215.
- [99] F.-K. Hsu, C.-W. Hsu, J.-K. Chang, C.-K. Lin, S.-L. Lee, C.-E. Jiang, *Int J Hydro Energy* 35 (24) (2010) 13247–13254.
- [100] S. Hai, X. Liu, W. Wang, Y. Liu, J. Li, *Int J Hydro Energy* 47 (47) (2022) 20604–20616.
- [101] Y. Zhang, H. Yang, H. Yuan, E. Yang, Z. Zhou, D. Song, *J Alloys Compd* 269 (1–2) (1998) 278–283.
- [102] W. Myers, L. Wang, T. Richardson, M. Rubin, *J Appl Phys* 91 (8) (2002) 4879–4885.
- [103] U. Häussermann, H. Blomqvist, D. Noréus, *Inorg Chem* 41 (14) (2002) 3684–3692.
- [104] J. Nylén, F.J. Garcìa Garcìà, B.D. Mosel, R. Pöttgen, U. Häussermann, *Solid State Sci* 6 (1) (2004) 147–155.